The Journal of Chemical Physics

Non-adiabatic ring polymer molecular dynamics with spin mapping variables

Cite as: J. Chem. Phys. **154**, 184106 (2021); https://doi.org/10.1063/5.0051456
Submitted: 25 March 2021 . Accepted: 26 April 2021 . Published Online: 12 May 2021

Duncan Bossion, Sutirtha N. Chowdhury, and Pengfei Huo

View Online Export Citation CrossMark

ARTICLES YOU MAY BE INTERESTED IN

Machine learning phase space quantum dynamics approaches
The Journal of Chemical Physics **154**, 184104 (2021); https://doi.org/10.1063/5.0046689

Non-adiabatic Matsubara dynamics and non-adiabatic ring-polymer molecular dynamics
The Journal of Chemical Physics **154**, 124124 (2021); https://doi.org/10.1063/5.0042136

Machine learning meets chemical physics
The Journal of Chemical Physics **154**, 160401 (2021); https://doi.org/10.1063/5.0051418

Challenge us.
What are your needs for periodic signal detection?
Watch
Zurich Instruments

AIP Publishing

© 2021 Author(s).

The Journal of Chemical Physics ARTICLE scitation.org/journal/jcp

Non-adiabatic ring polymer molecular dynamics with spin mapping variables

Cite as: J. Chem. Phys. 154, 184106 (2021); doi: 10.1063/5.0051456
Submitted: 25 March 2021 • Accepted: 26 April 2021 •
Published Online: 12 May 2021

View Online Export Citation CrossMark

Duncan Bossion,[1,a)] Sutirtha N. Chowdhury,[1] and Pengfei Huo[1,2,b)]

AFFILIATIONS

[1] Department of Chemistry, University of Rochester, 120 Trustee Road, Rochester, New York 14627, USA
[2] The Institute of Optics, Hajim School of Engineering, University of Rochester, Rochester, New York 14627, USA

[a)] E-mail: dbossion@ur.rochester.edu
[b)] Author to whom correspondence should be addressed: pengfei.huo@rochester.edu

ABSTRACT

We present a new non-adiabatic ring polymer molecular dynamics (NRPMD) method based on the spin mapping formalism, which we refer to as the spin mapping NRPMD (SM-NRPMD) approach. We derive the path-integral partition function expression using the spin coherent state basis for the electronic states and the ring polymer formalism for the nuclear degrees of freedom. This partition function provides an efficient sampling of the quantum statistics. Using the basic properties of the Stratonovich–Weyl transformation, we further justify a Hamiltonian that we propose for the dynamical propagation of the coupled spin mapping variables and the nuclear ring polymer. The accuracy of the SM-NRPMD method is numerically demonstrated by computing the nuclear position and population auto-correlation functions of non-adiabatic model systems. The results obtained using the SM-NRPMD method agree very well with the numerically exact results. The main advantage of using the spin mapping variables over the harmonic oscillator mapping variables is numerically demonstrated, where the former provides nearly time-independent expectation values of physical observables for systems under thermal equilibrium. We also explicitly demonstrate that SM-NRPMD provides invariant dynamics upon various ways of partitioning the state-dependent and state-independent potentials.

Published under license by AIP Publishing. https://doi.org/10.1063/5.0051456

I. INTRODUCTION

One of the central challenges in theoretical chemistry is to accurately simulate chemical reactions involving non-adiabatic processes and nuclear quantum effects.[1] These reactions, such as the electron transfer, the proton-coupled electron transfer, or the scattering reactions involving non-adiabatic transitions among many electronic states and nuclear quantum effects, are commonly encountered from photo-catalysis, biochemistry and enzymatic reactions, to astrochemistry. Developing accurate yet numerically efficient approaches has become a key focus in physical chemistry.

To this end, a large number of these approaches are developed, including the popular trajectory surface-hopping method (mixed quantum–classical approach),[2–5] the linearized semi-classical (LSC) path-integral approaches,[6,7] the partially linearized density matrix (PLDM) path-integral approaches,[8–11] the mixed quantum–classical Liouville equation,[12–15] and the symmetrical quasi-classical (SQC) approach,[16,17] to name a few. Despite their success, these approaches generally do not preserve the quantum detailed balance[18,19] or the zero-point energy (ZPE) associated with the nuclear degrees of freedom (DOFs) and often suffer from numerical issues, such as ZPE leakage.[20,21]

Imaginary-time path-integral approaches,[22–24] such as the ring polymer molecular dynamics (RPMD),[25,26] resemble classical dynamics in an extended phase space and provide a convenient way to compute approximate quantum time-correlation functions (TCFs).[25] The classical evolution of RPMD preserves its initial quantum distribution captured by the ring polymer Hamiltonian and is free of the ZPE leaking problem.[20,25] Despite its success in describing quantum effects in the condensed phase, RPMD is limited to one-electron non-adiabatic dynamics[27–31] or nuclear quantization[25,32–35] and is lacking real-time electronic coherence effects.[27,28]

Recently emerged state-dependent RPMD approaches, such as the non-adiabatic RPMD (NRPMD),[36–38] the mapping variable RPMD (MV-RPMD),[39,40] and the coherent state RPMD (CS-RPMD),[41] are promising to provide accurate non-adiabatic

Published under license by AIP Publishing

dynamics with an explicit description of electronic states, in addition to the reliable treatment of nuclear quantum effects through ring polymer quantization. The common ingredient of these approaches is the Meyer–Miller–Thoss–Stock (MMST) mapping formalism,[42–44] which maps N electronic states onto N singly excited harmonic oscillators. The electronic non-adiabatic dynamics is hence mapped onto the phase space trajectories of the mapping oscillators, which evolve together with the nuclear ring polymer. Hence, these MMST-based RPMD approaches can be viewed as unified theories of the mapping oscillators and the ring polymer. These methods are shown to provide both accurate non-adiabatic dynamics and nuclear quantum effects.[36–38] In particular, the NRPMD approach has been rigorously derived from the non-adiabatic Matsubara dynamics framework.[45]

One potential limitation of these state-dependent RPMD approaches is rooted in the MMST mapping representation. It is well known that the MMST representation has a larger size of Hilbert space than the original electronic subspace and requires a projection back to that subspace to obtain accurate results.[14,46] In addition, the total population along a single trajectory is not guaranteed to be unitary, hence breaking the dynamical invariance under different ways of partitioning the potentials into state-dependent and state-independent components when approximate quantum dynamics methods are used.[14,44,47] Besides the widely used MMST representation, there exist other mapping formalisms based upon spin coherent states.[48–52] In particular, a new spin mapping formalism[53,54] based on the Stratonovich–Weyl transform[55] was recently developed by Runeson and Richardson. In this spin mapping approach,[53] two electronic states are mapped onto two angles defining the spin coherent state on the Bloch sphere. One of the advantages of this approach, compared to the MMST formalism, is that the spin coherent state basis is of the same dimensionality as the electronic state basis of the original system; hence, it provides a more consistent mapping than the MMST approach and it does not require any additional projection back to the electronic subspace.[53] The spin mapping (SM) variables, being bounded to the Bloch sphere, also guarantee the total population along a single trajectory to be unitary. This further enforces the independence of the dynamics to the splitting between the state-dependent and state-independent parts of the Hamiltonian. It has been shown that in the LSC[53,54] and the PLDM[56,57] approaches, using the spin mapping formalism provides a more accurate non-adiabatic dynamics compared to the corresponding approaches when using the MMST formalism.[7,8] These exciting theoretical developments of the spin mapping variables have motivated us to develop an NRPMD approach using the spin mapping representation.

In this paper, we develop a new non-adiabatic RPMD method, which we refer to as the spin mapping NRPMD (SM-NRPMD), based on the recently developed spin mapping formalism.[53,54] We first derive a partition function based on the SM representation that allows one to efficiently sample the exact quantum statistics. We then propose the SM-NRPMD Hamiltonian for propagating dynamics. With the proposed SM-NRPMD approach, we compute the Kubo-transformed position and population auto-correlation functions with non-adiabatic model systems and demonstrate that this approach is capable of accurately describing both the correct quantum statistics and the electronic Rabi oscillations. Compared to the MMST-based NRPMD approaches,[58] SM-NRPMD seems to better preserve the quantum detailed balance, resulting in a nearly time-independent expectation value of the nuclear position or population for the system under thermal equilibrium. Finally, we demonstrate that the dynamics is invariant to the partitioning of the potential into state-dependent and state-independent components.

II. BASIC THEORY OF THE TWO-LEVEL SPIN MAPPING FORMALISM

In this section, we review the spin mapping formalism for electronic states introduced by Runeson and Richardson.[53,54] A comprehensive introduction of this material can be found in Ref. 53. In this paper, we focus on the spin mapping representation of two-level systems. Generalizing the theory to many states is possible by using the generators of the SU(N) Lie algebra,[54] and we plan to apply this formalism to develop a general SM-NRPMD approach in the future.

The total Hamiltonian operator of the system is

$$\hat{H} = \frac{\hat{P}^2}{2m}\hat{\mathcal{I}} + U_0(\hat{R})\hat{\mathcal{I}} + \begin{pmatrix} V_1(\hat{R}) & \Delta(\hat{R}) \\ \Delta(\hat{R}) & V_2(\hat{R}) \end{pmatrix}, \tag{1}$$

where $U_0(\hat{R})$ represents the state-independent potential energy operator and $\hat{R}$ and $\hat{P}$ are the position and momentum operators of the nuclear DOF, respectively. The Hamiltonian can also be written in terms of spin operators as[49]

$$\hat{H} = H_0\hat{\mathcal{I}} + \frac{1}{\hbar}\mathbf{H}\cdot\hat{\mathbf{S}} = H_0\hat{\mathcal{I}} + \frac{1}{\hbar}\left(H_x\cdot\hat{S}_x + H_y\cdot\hat{S}_y + H_z\cdot\hat{S}_z\right), \tag{2}$$

where $\hat{\mathcal{I}}$ is the 2×2 identity matrix and $\hat{S}_i = \frac{\hbar}{2}\hat{\sigma}_i$ (for $i \in \{x,y,z\}$) is the quantum spin operator, with the Pauli matrices $\hat{\sigma}_i$ expressed as follows:

$$\hat{\sigma}_x = \begin{pmatrix} 0 & 1 \\ 1 & 0 \end{pmatrix}, \quad \hat{\sigma}_y = \begin{pmatrix} 0 & -i \\ i & 0 \end{pmatrix}, \quad \hat{\sigma}_z = \begin{pmatrix} 1 & 0 \\ 0 & -1 \end{pmatrix}. \tag{3}$$

The different components of the Hamiltonian in Eq. (2) are expressed as

$$H_0 = \frac{\hat{P}^2}{2m} + U_0\left(\hat{R}\right) + \frac{1}{2}\left(V_1\left(\hat{R}\right) + V_2\left(\hat{R}\right)\right), \tag{4a}$$

$$H_x = 2\Re\left(\Delta\left(\hat{R}\right)\right), \tag{4b}$$

$$H_y = 2\Im\left(\Delta\left(\hat{R}\right)\right), \tag{4c}$$

$$H_z = V_1\left(\hat{R}\right) - V_2\left(\hat{R}\right), \tag{4d}$$

where $\Re$ and $\Im$ represent the real and imaginary components of any number, respectively. Note that for a molecular Hamiltonian, one often has $\Im(\Delta(\hat{R})) = 0$.

Following the original work on the spin mapping formalism,[53] we introduce the spin coherent state (SCS) basis[53,59]

Published under license by AIP Publishing

$$|\mathbf{u}\rangle = \cos\frac{\theta}{2}e^{-i\varphi/2}|1\rangle + \sin\frac{\theta}{2}e^{i\varphi/2}|2\rangle, \tag{5}$$

with the two angles, θ and φ, defining the state of spin of the system on the Bloch sphere. The SCS vector is normalized $\langle\mathbf{u}|\mathbf{u}\rangle = 1$. The expectation value of the spin operator is

$$S_i(\mathbf{u}) = \langle\mathbf{u}|\hat{S}_i|\mathbf{u}\rangle = \frac{\hbar}{2}u_i, \qquad i \in \{x, y, z\}, \tag{6}$$

where u_x, u_y, and u_z are expressed as follows:

$$u_x = \sin\theta\cos\varphi, \tag{7a}$$

$$u_y = \sin\theta\sin\varphi, \tag{7b}$$

$$u_z = \cos\theta. \tag{7c}$$

We further introduce three functions for the Stratonovich–Weyl (SW) transformation of any operator in the SM representation, named the Q-, P-, and W-functions. These functions depend on the *kernel* $\hat{w}_s$ and the *spin radius* r_s as follows:[53]

$$\hat{w}_s(\mathbf{u}) = \frac{1}{2}\hat{\mathcal{I}} + r_s\mathbf{u}\cdot\hat{\boldsymbol{\sigma}}, \qquad s \in \{Q, P, W\}, \tag{8a}$$

$$r_Q = \frac{1}{2}, \quad r_P = \frac{3}{2}, \quad r_W = \frac{\sqrt{3}}{2}, \tag{8b}$$

where $\mathbf{u}\cdot\hat{\boldsymbol{\sigma}} = u_x\cdot\hat{\sigma}_x + u_y\cdot\hat{\sigma}_y + u_z\cdot\hat{\sigma}_z$.

The SCS projection operator is $|\mathbf{u}\rangle\langle\mathbf{u}| = \cos^2\frac{\theta}{2}|1\rangle\langle 1| + \cos\frac{\theta}{2}\sin\frac{\theta}{2}e^{-i\varphi}|1\rangle\langle 2| + \cos\frac{\theta}{2}\sin\frac{\theta}{2}e^{i\varphi}|2\rangle\langle 1| + \sin^2\frac{\theta}{2}|2\rangle\langle 2|$. Note that

$$\hat{w}_Q = |\mathbf{u}\rangle\langle\mathbf{u}|, \tag{9}$$

which can be easily verified using elementary trigonometric identities. On the other hand, $\hat{w}_P$ and $\hat{w}_W$ do not have a simple relation with $|\mathbf{u}\rangle\langle\mathbf{u}|$.

A. Spin mapping of diabatic electronic states

The SW transform of an operator $\hat{A}$ is defined as

$$A_s(\mathbf{u}) \equiv \left[\hat{A}\right]_s(\mathbf{u}) = \mathrm{Tr}_e\left[\hat{A}\hat{w}_s\right], \tag{10}$$

where the trace is taken in the electronic subspace, which is equivalent to the two-state spin subspace.

Mapping an operator $\hat{A}$ onto the spin Hilbert subspace corresponds to the following relation:[53]

$$\hat{A} \to A_s(\mathbf{u}) = \mathrm{Tr}_e\left[\hat{A}\hat{w}_s\right]. \tag{11}$$

Generalizing the theory to many states is also possible[54] by using the generators of the SU(N) Lie algebra [when $N = 3$, it corresponds to the Gell-Mann matrices in the $SU(3)$-symmetry theory of quarks].

For the s ≡ Q special case, this mapping relation means that

$$A_Q(\mathbf{u}) = \mathrm{Tr}_e\left[\hat{A}\hat{w}_Q\right] = \mathrm{Tr}_e\left[\hat{A}|\mathbf{u}\rangle\langle\mathbf{u}|\right] = \langle\mathbf{u}|\hat{A}|\mathbf{u}\rangle. \tag{12}$$

The Q-relation maps the spin operator $\hat{S}_i$ with $[\hat{S}_i]_Q = \frac{\hbar}{2}u_i$, which is its expectation value in the SCS through Eq. (6).

Using the spin mapping defined in Eq. (11), it is easy to show that $[\hat{\mathcal{I}}]_s(\mathbf{u}) = 1$ (because $\mathrm{Tr}_e\hat{\sigma}_i = 0$ for all i), as well as

$$\mathbf{S}_s(\mathbf{u}) \equiv \left[\hat{\mathbf{S}}\right]_s(\mathbf{u}) = \mathrm{Tr}_e\left[\frac{\hbar}{2}\hat{\boldsymbol{\sigma}}\left(\frac{1}{2}\hat{\mathcal{I}} + r_s\mathbf{u}\cdot\hat{\boldsymbol{\sigma}}\right)\right] = \hbar r_s\mathbf{u}. \tag{13}$$

The projection operators are transformed as

$$[|1\rangle\langle 1|]_s(\mathbf{u}) = \left[\frac{1}{2}\hat{\mathcal{I}} + \frac{1}{\hbar}\hat{S}_z\right]_s(\mathbf{u}) = \frac{1}{2} + r_s\cos\theta, \tag{14a}$$

$$[|2\rangle\langle 2|]_s(\mathbf{u}) = \left[\frac{1}{2}\hat{\mathcal{I}} - \frac{1}{\hbar}\hat{S}_z\right]_s(\mathbf{u}) = \frac{1}{2} - r_s\cos\theta, \tag{14b}$$

$$[|1\rangle\langle 2| + |2\rangle\langle 1|]_s(\mathbf{u}) = 2\left[\frac{1}{\hbar}\hat{S}_x\right]_s(\mathbf{u}) = 2r_s\sin\theta\cos\varphi, \tag{14c}$$

$$[|1\rangle\langle 2| - |2\rangle\langle 1|]_s(\mathbf{u}) = 2i\left[\frac{1}{\hbar}\hat{S}_y\right]_s(\mathbf{u}) = 2ir_s\sin\theta\sin\varphi. \tag{14d}$$

The Hamiltonian in Eq. (2) is mapped as $\hat{H} \to [\hat{H}]_s(\mathbf{u})$ with the following expression:

$$\begin{aligned} H_s(\mathbf{u}) &\equiv \left[\hat{H}\right]_s(\mathbf{u}) = H_0 + r_s\mathbf{H}\cdot\mathbf{u} \\ &= \frac{P^2}{2m} + U_0 + \left(\frac{1}{2} + r_s\cos\theta\right)\cdot V_1 + \left(\frac{1}{2} - r_s\cos\theta\right)\cdot V_2 \\ &\quad + 2r_s\sin\theta\cos\varphi\cdot\Re(\Delta). \end{aligned} \tag{15}$$

In the case where the coupling is complex as investigated in Ref. 60, the additional term $2ir_s\sin\theta\sin\varphi\cdot\Im(\Delta)$is required in Eq. (15).

Note that H_0 and $\mathbf{H}$ are, in principle, R-dependent. The SW mapping is closely related to the MMST mapping approach, and a brief discussion between these two formalisms is provided in Appendix A, whereas a thorough comparison can be found in Ref. 53. Compared to another recent spin mapping formalism by Cotton and Miller,[61] as well as shown by Liu[62] from a unified mapping theory, the spin mapping used in the current work[53] maps two states onto one spin-$\frac{1}{2}$ particle, whereas the Cotton–Miller (CM) approach maps the two states onto two spin-$\frac{1}{2}$ particles. Thus, in the latter approach, there are more DOFs in the mapping space than in the original quantum system and so does the MMST mapping. Another important difference is that the CM spin mapping approach in Ref. 61 is not exact for pure electronic subsystem dynamics,[62] whereas the current spin mapping formalism gives the exact dynamics for the isolated electronic subsystem.

To obtain the equations of motion (EOMs) governed by $H_s(\mathbf{u})$ in Eq. (15) for the spin mapping variables, we start with the following Heisenberg EOM for $\hat{\mathbf{S}}$:

Published under license by AIP Publishing

$$\frac{d}{dt}\hat{\mathbf{S}} = \frac{1}{i\hbar}\left[\hat{\mathbf{S}}, \hat{H}\right] = \frac{1}{\hbar}\mathbf{H}(\hat{R}) \times \hat{\mathbf{S}}, \tag{16}$$

where $\times$ denotes the cross product of two vectors, and we have used the fact that $H_0\hat{\mathcal{I}}$ in $\hat{H}$ [Eq. (2)] is $\hat{\mathbf{S}}$-independent and, hence, commutes with $\hat{\mathbf{S}}$. Applying the SW transform [Eq. (10)] on both sides of the above equation, we have

$$\frac{d}{dt}\mathbf{u} = \frac{1}{\hbar}\mathbf{H}(\hat{R}) \times \mathbf{u}. \tag{17}$$

Note that the above equation is exact, regardless of the r_s-dependence of $\hat{H}$. Of course, the EOM for the nuclear DOF is not yet explicitly expressed. When choosing the Wigner representation for the nuclei and using the quantum–classical Liouville equation (QCLE),[53] Eq. (17) can also be rigorously derived. This equation can be solved by treating $\mathbf{u}$ as dynamical variables, or equivalently, θ and φ. Further analysis of this is provided in Appendix B.

B. Properties of the Stratonovich–Weyl transform

Here, we briefly summarize several basic properties of the SW transform, which will be used to derive the quantum partition function and the spin mapping NRPMD Hamiltonian in Sec. III. Using the spin mapping formalism, the quantum mechanical trace of an operator $\hat{A}$ in the Q-function is expressed as

$$\begin{aligned}\mathrm{Tr}_e\left[\hat{A}\right] &= \int d\mathbf{u}\langle\mathbf{u}|\hat{A}|\mathbf{u}\rangle = \int d\mathbf{u} A_Q(\mathbf{u}) \\ &= \frac{1}{2\pi}\int_0^\pi d\theta \sin\theta \int_0^{2\pi} d\varphi A_Q(\theta,\varphi),\end{aligned} \tag{18}$$

where $\int d\mathbf{u} = \frac{1}{2\pi}\int_0^\pi d\theta \sin\theta \int_0^{2\pi} d\varphi$. Note that because $\langle\mathbf{u}|\hat{A}\hat{B}|\mathbf{u}\rangle \neq \langle\mathbf{u}|\hat{A}|\mathbf{u}\rangle\langle\mathbf{u}|\hat{B}|\mathbf{u}\rangle$ (the uncertainty property), the Q-function cannot be used to directly compute the quantum mechanical trace of a product of operators, i.e., $\mathrm{Tr}_e\left[\hat{A}\hat{B}\right] \neq \int d\mathbf{u} A_Q(\mathbf{u}) B_Q(\mathbf{u})$.

To solve this issue, one can use the P-function and the following property:

$$\mathrm{Tr}_e\left[\hat{A}\hat{B}\right] = \int d\mathbf{u} A_Q(\mathbf{u}) B_P(\mathbf{u}) = \int d\mathbf{u} A_P(\mathbf{u}) B_Q(\mathbf{u}). \tag{19}$$

The W-function can also be used for this purpose and is self-dual,

$$\mathrm{Tr}_e\left[\hat{A}\hat{B}\right] = \int d\mathbf{u} A_W(\mathbf{u}) B_W(\mathbf{u}). \tag{20}$$

Summarizing the above properties, we have

$$\mathrm{Tr}_e\left[\hat{A}\hat{B}\right] = \int d\mathbf{u} A_s(\mathbf{u}) B_{\bar{s}}(\mathbf{u}), \tag{21}$$

where $\{s, \bar{s}\}$ can be $\{Q, P\}$, $\{P, Q\}$, or $\{W, W\}$. The proof of Eq. (21) is elementary and is provided in Appendix C.

Choosing $\hat{B} = \hat{\mathcal{I}}$, Eq. (21) becomes

$$\mathrm{Tr}_e\left[\hat{A}\right] = \int d\mathbf{u} A_s(\mathbf{u}) \left[\hat{\mathcal{I}}\right]_{\bar{s}}(\mathbf{u}) = \int d\mathbf{u} A_s(\mathbf{u}), \tag{22}$$

where we have used the fact that $\left[\hat{\mathcal{I}}\right]_{\bar{s}} = 1$. This suggests that, to evaluate the quantum mechanical trace of an operator $\hat{A}$, one can freely choose any $s \in \{Q, P, W\}$ index, even though each has a different kernel $\hat{w}_s$ and a different radius r_s, as they all give the correct result. Further using the definition of $A_s(\mathbf{u})$ [Eq. (11)] into Eq. (22), we have

$$\mathrm{Tr}_e\left[\hat{A}\right] = \int d\mathbf{u}\, \mathrm{Tr}_e\left[\hat{A}\hat{w}_s\right] = \mathrm{Tr}_e\left[\hat{A} \cdot \int d\mathbf{u}\hat{w}_s\right], \tag{23}$$

where we have moved the d$\mathbf{u}$ integral inside the trace (and note that $\hat{A}$ is $\mathbf{u}$-independent). The above equality indicates the following resolution of identity:

$$\begin{aligned}\mathbb{1}_{\mathbf{u}} &= \int d\mathbf{u}\hat{w}_s \\ &= \frac{1}{2\pi}\int_0^\pi d\theta \sin\theta \int_0^{2\pi} d\varphi\left(\frac{1}{2}\hat{\mathcal{I}} + r_s\mathbf{u}\cdot\hat{\boldsymbol{\sigma}}\right),\end{aligned} \tag{24}$$

where, to obtain the second line of the above equation, we used the expressions of $\int d\mathbf{u}$ [Eq. (18)] and $\hat{w}_s$ [Eq. (8a)]. This identity can also be easily verified through elementary integrals, which is provided in Appendix C.

When choosing $s \equiv Q$, the resolution of identity is

$$\mathbb{1}_{\mathbf{u}} = \int d\mathbf{u}\hat{w}_Q = \int d\mathbf{u}|\mathbf{u}\rangle\langle\mathbf{u}|, \tag{25}$$

where we used $\hat{w}_Q = |\mathbf{u}\rangle\langle\mathbf{u}|$.

III. QUANTUM PARTITION FUNCTION WITH SPIN MAPPING VARIABLES

A. Spin coherent state (SCS) partition function

The canonical partition function is expressed as $\mathcal{Z} = \mathrm{Tr}_n\,\mathrm{Tr}_e\left[e^{-\beta\hat{H}}\right]$, where Tr_n and Tr_e represent the traces over the nuclear and electronic DOFs, respectively, and $\beta = 1/k_B T$. The partition function can be exactly evaluated in the limit $N \to \infty$ by the Trotter discretization,[63] where N is the number of ring polymer beads.

We start from expressing the quantum partition function as follows:

$$\mathcal{Z} = \mathrm{Tr}_e\,\mathrm{Tr}_n\left[\left(e^{-\beta_N\left(H_0\hat{\mathcal{I}} + \frac{1}{\hbar}\mathbf{H}\cdot\hat{\mathbf{S}}\right)}\right)^N\right], \tag{26}$$

where $\beta_N = \beta/N$. Inserting N copies of the identity in the nuclear subspace, $\mathbb{1}_R = \int dR_\alpha |R_\alpha\rangle\langle R_\alpha|$ and $\mathbb{1}_P = \int dP_\alpha |P_\alpha\rangle\langle P_\alpha|$, where α is the label of the imaginary-time slice (bead) index, and using the standard path-integral techniques,[22,23,64] we obtain

$$\mathcal{Z} = \frac{1}{(2\pi\hbar)^N}\lim_{N\to\infty}\int d\{R_\alpha\}\int d\{P_\alpha\} e^{-\beta_N\tilde{H}_0(\mathbf{R})}\mathrm{Tr}_e\left[\prod_{\alpha=1}^N e^{-\beta_N\frac{1}{\hbar}\mathbf{H}_\alpha\cdot\hat{\mathbf{S}}}\right]. \tag{27}$$

Here, we use the notation $\int d\{X_\alpha\} = \prod_{\alpha=1}^N \int dX_1, \ldots, dX_N$, $\mathbf{R} \equiv \{R_\alpha\}$, and $\mathbf{H}_\alpha = [H_x(R_\alpha), H_y(R_\alpha), H_z(R_\alpha)]$ [see their definitions in Eqs. (4b)–(4d)]. The state-independent ring polymer Hamiltonian $\tilde{H}_0$ is expressed as

Published under license by AIP Publishing

$$\tilde{H}_0(\mathbf{R}) = \sum_{\alpha=1}^{N}\Big[\frac{P_\alpha^2}{2m} + \frac{m}{2\beta_N^2\hbar^2}(R_\alpha - R_{\alpha-1})^2 + U_0(R_\alpha) + \frac{1}{2}(V_1(R_\alpha) + V_2(R_\alpha))\Big]. \tag{28}$$

To perform the electronic trace, we insert N copies of the spin coherent state identity (by choosing s ≡ Q)

$$\mathbb{1}_{\mathbf{u}} = \int \mathrm{d}\mathbf{u}_\alpha |\mathbf{u}_\alpha\rangle\langle\mathbf{u}_\alpha| = \int \mathrm{d}\mathbf{u}_\alpha \hat{w}_{\mathrm{Q}} \tag{29a}$$

$$= \frac{1}{2\pi}\int_0^\pi \mathrm{d}\theta_\alpha \sin\theta_\alpha \int_0^{2\pi} \mathrm{d}\varphi_\alpha |\mathbf{u}_\alpha\rangle\langle\mathbf{u}_\alpha| \tag{29b}$$

and rearrange the terms (as well as neglecting a normalization constant), resulting in

$$\mathcal{Z} \propto \lim_{N\to\infty} \int \mathrm{d}\{R_\alpha\} \int \mathrm{d}\{P_\alpha\} \int \mathrm{d}\{\mathbf{u}_\alpha\} e^{-\beta_N \tilde{H}_0(\mathbf{R})} \times \prod_{\alpha=1}^{N} \langle \mathbf{u}_\alpha | e^{-\beta_N \frac{1}{\hbar}\mathbf{H}_\alpha\cdot\hat{\mathbf{S}}} | \mathbf{u}_{\alpha+1}\rangle. \tag{30}$$

The above partition function can also be equivalently expressed by inserting electronic projection operators $\hat{\mathcal{P}} = \sum_n |n\rangle\langle n|$, leading to

$$\mathcal{Z} \propto \lim_{N\to\infty} \int \mathrm{d}\{R_\alpha\} \int \mathrm{d}\{P_\alpha\} \int \mathrm{d}\{\mathbf{u}_\alpha\} e^{-\beta_N \tilde{H}_0(\mathbf{R})} \times \prod_{\alpha=1}^{N} \langle \mathbf{u}_\alpha | \sum_n |n\rangle\langle n| e^{-\beta_N \frac{1}{\hbar}\mathbf{H}_\alpha\cdot\hat{\mathbf{S}}} \sum_m |m\rangle\langle m| \mathbf{u}_{\alpha+1}\rangle. \tag{31}$$

Note that the size of the spin mapping Hilbert space $\mathbb{1}_{\mathbf{u}}$ is the same as the original electronic subspace $\hat{\mathcal{P}} = \sum_n |n\rangle\langle n|$. Hence, with or without $\hat{\mathcal{P}}$, the partition function is invariant. This is different than the mapping in harmonic oscillators based on the MMST formalism, where the mapping Hilbert space is larger than the original electronic subspace and where projections often lead to a better result.[14,46]

We further express the matrix elements of the spin coherent state projected by $\hat{\mathcal{P}}$ as

$$\mathbf{C}(\mathbf{u}_\alpha) \equiv \langle \mathbf{u}_\alpha | \sum_n |n\rangle\langle n| = \cos\frac{\theta_\alpha}{2} e^{i\frac{\varphi_\alpha}{2}} \langle 1| + \sin\frac{\theta_\alpha}{2} e^{-i\frac{\varphi_\alpha}{2}} \langle 2|, \tag{32a}$$

$$\mathbf{D}(\mathbf{u}_{\alpha+1}) \equiv \sum_m |m\rangle\langle m|\mathbf{u}_{\alpha+1}\rangle = \cos\frac{\theta_{\alpha+1}}{2} e^{-i\frac{\varphi_{\alpha+1}}{2}} |1\rangle + \sin\frac{\theta_{\alpha+1}}{2} e^{i\frac{\varphi_{\alpha+1}}{2}} |2\rangle. \tag{32b}$$

Using these, we can write the special form of the Spin Coherent State (SCS) partition function (with s ≡ Q case) as follows:

$$\mathcal{Z} \propto \lim_{N\to\infty} \int \mathrm{d}\{R_\alpha\} \int \mathrm{d}\{P_\alpha\} \int \mathrm{d}\{\mathbf{u}_\alpha\} \mathrm{Tr}_{\mathrm{e}}[\mathbf{\Gamma}_{\mathrm{Q}}] \cdot e^{-\beta_N \tilde{H}_0(\mathbf{R})}, \tag{33}$$

where the electronic trace has the following expression:

$$\mathbf{\Gamma}_{\mathrm{Q}} = \prod_{\alpha=1}^{N} \sum_{n,m} C_n(\mathbf{u}_\alpha) \mathcal{M}_{nm}(R_\alpha) D_m(\mathbf{u}_{\alpha+1}), \tag{34a}$$

$$\mathcal{M}_{nm}(R_\alpha) = \langle n| e^{-\beta_N \frac{1}{\hbar}\mathbf{H}_\alpha\cdot\hat{\mathbf{S}}} |m\rangle. \tag{34b}$$

This partition function is analogous to those used with MMST mapping variables, such as the mapping-variable RPMD partition function[39] or the coherent state mapping ring polymer partition function.[41] In the latter, a similar derivation procedure is conducted with the coherent-state representation of the MMST mapping oscillators.[41,65]

The above procedure relies on inserting N copies of the identity $\mathbb{1}_{\mathbf{u}} = \int \mathrm{d}\mathbf{u}_\alpha |\mathbf{u}_\alpha\rangle\langle\mathbf{u}_\alpha| \equiv \int \mathrm{d}\mathbf{u}_\alpha \hat{w}_{\mathrm{Q}}(\mathbf{u}_\alpha)$ (where α is the bead index). Of course, one can insert the general resolution of identity $\mathbb{1}_{\mathbf{u}} = \int \mathbf{du}\hat{w}_{\tilde{\mathrm{s}}}$ [Eq. (24)] inside the $\mathrm{Tr}_{\mathrm{e}}[\cdots]$ of Eq. (27); then, by moving the $\int \mathrm{d}\mathbf{u}_\alpha$ integral outside Tr_{e}, it results in

$$\mathcal{Z} \propto \lim_{N\to\infty} \int \mathrm{d}\{R_\alpha\} \int \mathrm{d}\{P_\alpha\} \int \mathrm{d}\{\mathbf{u}_\alpha\} \mathrm{Tr}_{\mathrm{e}}[\mathbf{\Gamma}_{\mathrm{s}}] \cdot e^{-\beta_N \tilde{H}_0(\mathbf{R})}, \tag{35}$$

where the expression of the electronic trace is

$$\mathbf{\Gamma}_{\mathrm{s}} = \prod_{\alpha=1}^{N} e^{-\beta_N \frac{1}{\hbar}\mathbf{H}_\alpha\cdot\hat{\mathbf{S}}} \cdot \hat{w}_{\mathrm{s}}(\mathbf{u}_\alpha). \tag{36}$$

By Taylor expanding the Boltzmann operator and using the properties of the Pauli matrices, we can prove the following identity:

$$e^{-\beta_N \frac{1}{\hbar}\mathbf{H}_\alpha\cdot\hat{\mathbf{S}}} = \cosh\frac{\beta_N|\mathbf{H}_\alpha|}{2}\hat{\mathcal{I}} - \sinh\frac{\beta_N|\mathbf{H}_\alpha|}{2} \cdot \frac{2\mathbf{H}_\alpha\cdot\hat{\mathbf{S}}}{\hbar|\mathbf{H}_\alpha|}, \tag{37}$$

where $|\mathbf{H}_\alpha| = \sqrt{H_x^2(R_\alpha) + H_y^2(R_\alpha) + H_z^2(R_\alpha)}$. Plugging this identity back into Eq. (36), we obtain the general expression for $\mathbf{\Gamma}_{\mathrm{s}}$ as follows:

$$\mathbf{\Gamma}_{\mathrm{s}} = \Bigg[\prod_{\alpha=1}^{N}\Bigg(\frac{1}{2}\cosh\frac{\beta_N|\mathbf{H}_\alpha|}{2} - r_{\mathrm{s}}\frac{\mathbf{H}_\alpha}{|\mathbf{H}_\alpha|}\cdot\mathbf{u}_\alpha \sinh\frac{\beta_N|\mathbf{H}_\alpha|}{2}\Bigg)\hat{\mathcal{I}} + \Bigg(r_{\mathrm{s}}\mathbf{u}_\alpha \cosh\frac{\beta_N|\mathbf{H}_\alpha|}{2} - \frac{1}{|\mathbf{H}_\alpha|}\Big(\frac{\mathbf{H}_\alpha}{2} + ir_{\mathrm{s}}\mathbf{H}_\alpha\times\mathbf{u}_\alpha\Big) \times \sinh\frac{\beta_N|\mathbf{H}_\alpha|}{2}\Bigg)\cdot\hat{\boldsymbol{\sigma}}\Bigg]. \tag{38}$$

A detailed derivation of Eqs. (37) and (38) is provided in Appendix D. When s ≡ Q, Eq. (38) is equivalent to the expression of $\mathbf{\Gamma}_{\mathrm{Q}}$ in Eq. (33). The numerical advantage of Eq. (38) is that it replaces the $\mathcal{M}_{nm}(R_\alpha)$ matrix in Eq. (34b) with an analytic expression in Eq. (37).

B. Spin mapping (SM)-NRPMD Hamiltonian

The SCS-partition function in Eq. (35) gives the exact quantum statistics for a non-adiabatic system. The effective Hamiltonian from the SCS-partition function can be used to propagate the dynamics. However, it will not provide accurate electronic dynamics (such as

Published under license by AIP Publishing

electronic Rabi oscillation) due to the inter-bead coupling among the different electronic and nuclear DOFs in $\mathbf{\Gamma}_s$.

Instead of proposing a reasonable Hamiltonian for the dynamics propagation, we try to theoretically justify a Hamiltonian from an alternative expression of the partition function. To this end, we evaluate the electronic trace in Eq. (27) using the property $\mathrm{Tr}_e[\hat{A}] = \int d\mathbf{u} A_s(\mathbf{u})$ in Eq. (22), leading to

$$\mathrm{Tr}_e\left[\prod_{\alpha=1}^{N} e^{-\beta_N \frac{1}{\hbar}\mathbf{H}_\alpha\cdot\hat{\mathbf{S}}}\right] = \int d\mathbf{u}_1 \left[\prod_{\alpha=1}^{N} e^{-\beta_N \frac{1}{\hbar}\mathbf{H}_\alpha\cdot\hat{\mathbf{S}}}\right]_s(\mathbf{u}_1), \tag{39}$$

where $s \in \{Q, P, W\}$. We further separate $\prod_{\alpha=1}^{N} e^{-\beta_N \frac{1}{\hbar}\mathbf{H}_\alpha\cdot\hat{\mathbf{S}}}$ into $e^{-\beta_N \frac{1}{\hbar}\mathbf{H}_1\cdot\hat{\mathbf{S}}}\prod_{\alpha=2}^{N} e^{-\beta_N \frac{1}{\hbar}\mathbf{H}_\alpha\cdot\hat{\mathbf{S}}}$ and use the property expressed in Eq. (21), leading to

$$\begin{aligned}&\int d\mathbf{u}_1 \left[e^{-\beta_N \frac{1}{\hbar}\mathbf{H}_1\cdot\hat{\mathbf{S}}}\prod_{\alpha=2}^{N} e^{-\beta_N \frac{1}{\hbar}\mathbf{H}_\alpha\cdot\hat{\mathbf{S}}}\right]_s(\mathbf{u}_1)\\ &= \int d\mathbf{u}_1 \left[e^{-\beta_N \frac{1}{\hbar}\mathbf{H}_1\cdot\hat{\mathbf{S}}}\right]_s(\mathbf{u}_1)\cdot\left[\prod_{\alpha=2}^{N} e^{-\beta_N \frac{1}{\hbar}\mathbf{H}_\alpha\cdot\hat{\mathbf{S}}}\right]_{\bar{s}}(\mathbf{u}_1),\end{aligned} \tag{40}$$

where $\{s, \bar{s}\}$ can be any pair that is permitted based on Eq. (21).

To evaluate $[e^{-\beta_N \frac{1}{\hbar}\mathbf{H}_1\cdot\hat{\mathbf{S}}}]_s(\mathbf{u}_1)$, we Taylor expand the exponential and neglect the terms of order equal to or higher than β_N^2 (which is exact under the limit $N \to \infty$), leading to

$$\begin{aligned}\left[1 - \beta_N \frac{1}{\hbar}\mathbf{H}_1\cdot\hat{\mathbf{S}} + \mathcal{O}(\beta_N^2)\right]_s(\mathbf{u}_1) &= \exp[-\beta_N \cdot \frac{1}{\hbar}\mathbf{H}_1\cdot[\hat{\mathbf{S}}]_s(\mathbf{u}_1)]\\ &= \exp\left[-\beta_N \cdot \frac{1}{\hbar} r_s \mathbf{H}_1\cdot\mathbf{u}_1\right].\end{aligned} \tag{41}$$

Putting it back into Eq. (40), we have

$$\begin{aligned}\mathrm{Tr}_e\left[\prod_{\alpha=1}^{N} e^{-\beta_N \frac{1}{\hbar}\mathbf{H}_\alpha\cdot\hat{\mathbf{S}}}\right] &= \int d\mathbf{u}_1 e^{-\beta_N\cdot r_s\mathbf{H}_1\cdot\mathbf{u}_1}\cdot\left[\prod_{\alpha=2}^{N} e^{-\beta_N \frac{1}{\hbar}\mathbf{H}_\alpha\cdot\hat{\mathbf{S}}}\right]_{\bar{s}}(\mathbf{u}_1)\\ &= \int d\mathbf{u}_1 e^{-\beta_N\cdot r_s\mathbf{H}_1\cdot\mathbf{u}_1}\cdot\mathrm{Tr}_e\left[\prod_{\alpha=2}^{N} e^{-\beta_N \frac{1}{\hbar}\mathbf{H}_\alpha\cdot\hat{\mathbf{S}}}\hat{w}_{\bar{s}}(\mathbf{u}_1)\right].\end{aligned} \tag{42}$$

Further inserting the identity $\int d\mathbf{u}_2 \hat{w}_s(\mathbf{u}_2)$ [see Eq. (24)] inside the Tr_e, we have

$$\begin{aligned}&\mathrm{Tr}_e\left[\prod_{\alpha=1}^{N} e^{-\beta_N \frac{1}{\hbar}\mathbf{H}_\alpha\cdot\hat{\mathbf{S}}}\right]\\ &= \int d\mathbf{u}_1 e^{-\beta_N\cdot r_s\mathbf{H}_1\cdot\mathbf{u}_1}\cdot\mathrm{Tr}_e\left[\int d\mathbf{u}_2 \hat{w}_s(\mathbf{u}_2) e^{-\beta_N \frac{1}{\hbar}\mathbf{H}_2\cdot\hat{\mathbf{S}}}\prod_{\alpha=3}^{N} e^{-\beta_N \frac{1}{\hbar}\mathbf{H}_\alpha\cdot\hat{\mathbf{S}}}\hat{w}_{\bar{s}}(\mathbf{u}_1)\right]\\ &= \int d\mathbf{u}_1 e^{-\beta_N\cdot r_s\mathbf{H}_1\cdot\mathbf{u}_1}\int d\mathbf{u}_2\left[e^{-\beta_N \frac{1}{\hbar}\mathbf{H}_2\cdot\hat{\mathbf{S}}}\prod_{\alpha=3}^{N} e^{-\beta_N \frac{1}{\hbar}\mathbf{H}_\alpha\cdot\hat{\mathbf{S}}}\hat{w}_{\bar{s}}(\mathbf{u}_1)\right]_s(\mathbf{u}_2)\\ &= \int d\mathbf{u}_1 e^{-\beta_N\cdot r_s\mathbf{H}_1\cdot\mathbf{u}_1}\int d\mathbf{u}_2 e^{-\beta_N\cdot r_s\mathbf{H}_2\cdot\mathbf{u}_2}\mathrm{Tr}_e\left[\prod_{\alpha=3}^{N} e^{-\beta_N \frac{1}{\hbar}\mathbf{H}_\alpha\cdot\hat{\mathbf{S}}}\hat{w}_{\bar{s}}(\mathbf{u}_1)\hat{w}_{\bar{s}}(\mathbf{u}_2)\right],\end{aligned} \tag{43}$$

where in the second equality, we moved the $\int d\mathbf{u}_2$ outside the Tr_e, as well as used the definition of $[\hat{A}]_s(\mathbf{u})$ in Eq. (11). In the third equality, we have used the property previously used in Eq. (40).

Repeating the above argument for all N beads, we obtain the following partition function:

$$\mathcal{Z} \propto \lim_{N\to\infty}\int d\{R_\alpha\}\int d\{P_\alpha\}\int d\{\mathbf{u}_\alpha\}\Phi_{\bar{s}}\cdot e^{-\beta_N \tilde{H}_s}, \tag{44}$$

where $\Phi_{\bar{s}} = \mathrm{Tr}_e[\prod_{\alpha=1}^{N}\hat{w}_{\bar{s}}(\mathbf{u}_\alpha)]$, and the spin mapping (SM)-NRPMD Hamiltonian is

$$\tilde{H}_s = \tilde{H}_0(\mathbf{R}) + \sum_{\alpha=1}^{N} r_s \mathbf{H}_\alpha\cdot\mathbf{u}_\alpha, \tag{45}$$

which is the ring polymer generalization of $H_s(\mathbf{u})$ in Eq. (15) [with the additional ring polymer potential in Eq. (28)]. Based on our previous experience with the MMST version of the NRPMD approach, we conjecture that $\tilde{H}_s$ should be the Hamiltonian for the NRPMD propagation when using the spin mapping variables. This is because the correct EOM for the MMST mapping variables[45,47] can be derived based on the partition function[38] through a similar procedure as above, which coincides with the Liouvillian derived from the generalized Kubo-transformed TCF with the Matsubara approximation and ring polymer approximation.[45] We also note that, in principle, the partition function in Eq. (44) should generate the same result as the one in Eq. (35) under the limit $N \to \infty$. However, with a finite N, we find that the numerical convergence using Eq. (44) is much slower compared to Eq. (35), likely due to the limit we took in Eq. (41) (which requires a large N). Hence, we emphasize that Eq. (44) is only used as a justification for the Stratonovich–Weyl NRPMD Hamiltonian in Eq. (45) and not used for sampling the quantum initial distribution.

IV. SPIN MAPPING (SM)-NRPMD TIME-CORRELATION FUNCTION

The Kubo-transform real-time-correlation function for two operators $\hat{A}$ and $\hat{B}$ is expressed as

$$C_{AB}^{K}(t) = \frac{1}{\mathcal{Z}\beta}\int_0^\beta d\lambda\,\mathrm{Tr}\left[e^{-(\beta-\lambda)\hat{H}}\hat{A}e^{-\lambda\hat{H}}e^{i\hat{H}t/\hbar}\hat{B}e^{-i\hat{H}t/\hbar}\right]. \tag{46}$$

We propose that the above Kubo-transformed TCF [Eq. (46)] can be approximated as follows:

$$\begin{aligned}C_{AB}(t) = \frac{1}{\mathcal{Z}}\lim_{N\to\infty}&\int d\{R_\alpha\}\int d\{P_\alpha\}\int d\{\mathbf{u}_\alpha\}\\ &\times \mathrm{Tr}_e[\mathbf{\Gamma}_s]e^{-\beta_N\tilde{H}_0}[A]_N(0)[B]_N(t),\end{aligned} \tag{47}$$

where $[A]_N(0) = \frac{1}{N}\sum_{\alpha=1}^{N}A(R_\alpha) \equiv \bar{A}(0)$ and $[B]_N(t) = \frac{1}{N}\sum_{\alpha=1}^{N}B(R_\alpha(t)) \equiv \bar{B}(t)$ for $\hat{A}(\hat{R})$ and $\hat{B}(\hat{R})$ when they are functions of $\hat{R}$. When operators $\hat{A}$ and $\hat{B}$ are related to the electronic DOF, the TCF is proposed as

$$\begin{aligned}C_{AB}(t) = \frac{1}{\mathcal{Z}}\lim_{N\to\infty}&\int d\{R_\alpha\}\int d\{P_\alpha\}\int d\{\mathbf{u}_\alpha\}\\ &\times \mathrm{Tr}_e[\mathbf{\Gamma}_s\hat{A}]e^{-\beta_N\tilde{H}_0}[B_{\bar{s}}]_N(t),\end{aligned} \tag{48}$$

Published under license by AIP Publishing

with $\{s, \bar{s}\}$ being complementary indexes permitted by Eq. (21) in order to satisfy the requirement at $t = 0$ to compute the trace of two operators (i.e., $e^{-\beta H}\hat{A}$ and $\hat{B}$). The population estimator $\mathcal{P}^{s}_{nn}$ for the operator $\hat{A} = |n\rangle\langle n|$ is obtained with $\mathrm{Tr}_e[\mathbf{\Gamma}_s|n\rangle\langle n|]$, which one can write in a bead-averaged fashion as

$$\begin{aligned}\mathcal{P}^{s}_{nn} &= \mathrm{Tr}_e[\mathbf{\Gamma}_s|n\rangle\langle n|] \\ &= \frac{1}{N}\sum_{\mu=1}^{N}\Bigg[\prod_{\alpha'=1}^{N-\mu} e^{-\beta_N \frac{1}{\hbar}\mathbf{H}_{\alpha'}\cdot\hat{\mathbf{S}}}\cdot \hat{w}_s(\mathbf{u}_{\alpha'}) \\ &\quad \times |n\rangle\langle n| \prod_{\alpha''=N-\mu+1}^{N} e^{-\beta_N \frac{1}{\hbar}\mathbf{H}_{\alpha''}\cdot\hat{\mathbf{S}}}\cdot \hat{w}_s(\mathbf{u}_{\alpha''})\Bigg],\end{aligned} \tag{49}$$

to improve the statistical convergence. The analytic expression can be evaluated in the same way as $\mathbf{\Gamma}_s$ in Eq. (38), leading to $|n\rangle\langle n|$ inserted in between the α and the $\alpha + 1$ bead. Specifically, for $s \equiv Q$, using Eq. (34a), we have

$$\mathcal{P}^{Q}_{nn} = \frac{1}{N}\sum_{\alpha=1}^{N}\frac{\sum_m C_n(\mathbf{u}_\alpha)\mathcal{M}_{nm}(R_\alpha)D_m(\mathbf{u}_{\alpha+1})}{\sum_{n,m} C_n(\mathbf{u}_\alpha)\mathcal{M}_{nm}(R_\alpha)D_m(\mathbf{u}_{\alpha+1})}. \tag{50}$$

The population estimator for the operator $\hat{B}$ is obtained by

$$[B_{\bar{s}}]_N = \frac{1}{N}\sum_{\alpha=1}^{N} B_{\bar{s}}(\mathbf{u}_\alpha), \tag{51}$$

where $B_{\bar{s}}(\mathbf{u}_\alpha)$ is the SW transform of $\hat{B}$, and when $\hat{B} = |n\rangle\langle n|$, it is expressed as

$$B_{\bar{s}}(\mathbf{u}_\alpha) = \mathrm{Tr}_e[|n\rangle\langle n|\hat{w}_{\bar{s}}] = \begin{cases} 1/2 + r_{\bar{s}}\cos\theta_\alpha, & n = 1 \\ 1/2 - r_{\bar{s}}\cos\theta_\alpha, & n = 2. \end{cases}$$

The function $[B]_N(t)$ or $[B_{\bar{s}}]_N(t)$ is evaluated along the classical trajectory $\{R_\alpha(t), \mathbf{u}_\alpha(t)\}$, and the dynamics is *proposed* to be governed by

$$\tilde{H}_{\bar{s}} = \tilde{H}_0(\mathbf{R}) + \sum_{\alpha=1}^{N} r_{\bar{s}}\mathbf{H}(R_\alpha)\cdot\mathbf{u}_\alpha, \tag{52}$$

where the Hamiltonian is justified in Eq. (45). The EOMs are expressed as

$$\dot{R}_\alpha = \frac{\partial \tilde{H}_{\bar{s}}}{\partial P_\alpha} = \frac{P_\alpha}{m}, \tag{53a}$$

$$\dot{P}_\alpha = -\frac{\partial \tilde{H}_{\bar{s}}}{\partial R_\alpha} = -\frac{\partial \tilde{H}_0}{\partial R_\alpha} - r_{\bar{s}}\frac{\partial \mathbf{H}(R_\alpha)}{\partial R_\alpha}\cdot\mathbf{u}_\alpha, \tag{53b}$$

$$\dot{\mathbf{u}}_\alpha = \frac{1}{\hbar}\mathbf{H}(R_\alpha)\times\mathbf{u}_\alpha. \tag{53c}$$

In the original NRPMD method, the corresponding EOMs were first proposed[36] and were then recently proved through the nonadiabatic Matsubara dynamics formalism.[45] We envision that the above EOMs [Eqs. (53a)–(53c)] can also be proved in a similar way when using the spin mapping variables, and we will explore this in future studies.

V. COMPUTATIONAL DETAILS

To test the performances of the derived SCS-partition function in Eq. (35) [with the $\mathbf{\Gamma}_s$ expression in Eq. (38)], we adapt a widely used model system[46,66,67] and compute the state-dependent nuclear probability distribution. The model Hamiltonian is $\hat{H} = \hat{P}^2/2m + \hat{V}$, with nuclear mass $M = 3600$ a.u., and the diabatic potential $\hat{V}$ is defined as

$$V_{ij} = \begin{cases} \frac{1}{2}k_i(R - R_i)^2 + \epsilon_i, & i = j \\ 5\times 10^{-5}e^{-0.4R^2}, & i \neq j, \end{cases} \tag{54}$$

where the model parameters are presented in Table I. We refer to this model as model 0. The physical temperature of the system is set to $T = 8$ K.

The initial quantum distribution is sampled using the Metropolis–Hastings algorithm according to the following distribution function:

$$\rho(\{R_\alpha, \mathbf{u}_\alpha\}) = |\mathrm{Tr}_e[\mathbf{\Gamma}_s]|\cdot e^{-\beta_N \tilde{H}_0(\mathbf{R})} \tag{55}$$

with a complex weighting factor of

$$\Xi_s(\{R_\alpha, \mathbf{u}_\alpha\}) = \mathrm{Tr}_e[\mathbf{\Gamma}_s]/|\mathrm{Tr}_e[\mathbf{\Gamma}_s]|. \tag{56}$$

The nuclear probability distribution is obtained by computing

$$\begin{aligned}\mathrm{P}(R_0) &= \frac{\mathrm{Tr}\left[e^{-\beta\hat{H}}\,\delta(\hat{R} - R_0)\right]}{\mathcal{Z}} \\ &= \frac{1}{\langle\Re(\Xi_s)\rangle}\cdot\langle\Re(\Xi_s)\cdot\delta(R - R_0)\rangle,\end{aligned} \tag{57}$$

where $\mathrm{Tr} = \mathrm{Tr}_n\,\mathrm{Tr}_e$ (trace over both nuclear and electronic DOFs) and the bracket $\langle\cdots\rangle$ indicates an ensemble average with respect to $\rho(\{R_\alpha, \mathbf{u}_\alpha\})$ in Eq. (55). The state-resolved probability distribution is obtained by projecting the distribution onto a given state $|n\rangle\langle n|$, leading to the probability

$$\begin{aligned}\mathrm{P}_n(R_0) &= \frac{\mathrm{Tr}\left[e^{-\beta\hat{H}}|n\rangle\langle n|\delta(\hat{R} - R_0)\right]}{\mathcal{Z}} \\ &= \frac{1}{\langle\Re(\Xi_s)\rangle}\cdot\langle\Re(\Xi_s\cdot\mathcal{P}^{s}_{nn})\cdot\delta(R - R_0)\rangle,\end{aligned} \tag{58}$$

TABLE I. Parameters for model 0.

i	1	2
k_i	4×10^{-5}	3.2×10^{-5}
R_i	−1.75	1.75
ϵ_i	0.0	2.28×10^{-5}

Published under license by AIP Publishing

with the estimator $\mathcal{P}^{s}_{nn}$ expressed in Eq. (49). To compute $P(R_0)$ and $P_n(R_0)$, $N = 10$ beads were required to converge the results using a total of 2.4×10^7 configurations sampled from the Monte Carlo (MC) procedure for s ≡ Q. Exactly identical results can be obtained with the same bead-convergence for other choices of s, but the required number of configurations to achieve the same level of convergence is much higher. In particular, for $N = 10$ beads, using s ≡ W requires 24 times more trajectories, while using s ≡ P requires almost 2000 times more trajectories.

To assess the accuracy of the SM-NRPMD approach, we compute TCFs and compare our results with numerically exact Kubo-transformed quantum TCFs, as well as TCFs computed with a non-adiabatic RPMD approach based on the MMST formalism[36] and a mean-field method, the mean-field RPMD (MF-RPMD).[39,68] The model used for those calculations is a simple two-level system linearly coupled to a harmonic potential

$$\hat{H} = \frac{\hat{P}^2}{2m} + \frac{1}{2}m\omega^2\hat{R}^2 + \begin{pmatrix} \hat{R}+\epsilon & \Delta \\ \Delta & -\hat{R}-\epsilon \end{pmatrix}, \tag{59}$$

where Δ is the constant electronic coupling and 2ϵ is the energy bias between the two electronic states. We choose $m = \hbar = \omega = \beta = 1$ and the rest of the parameters are provided in Table II, changing the non-adiabaticity of the system from adiabatic (model I with $\beta\Delta = 10$) to highly non-adiabatic (model VII with $\beta\Delta = 0.1$). The number of beads required to generate the converged results is also provided in Table II.

The position and population auto-correlation functions are computed as follows:

$$C_{RR}(t) = \frac{1}{\langle \Re(\Xi_s)\rangle} \cdot \langle \Re(\Xi_s) \cdot \bar{R}(0) \cdot \bar{R}(t)\rangle, \tag{60}$$

$$C_{nn}(t) = \frac{1}{\langle \Re(\Xi_s)\rangle} \langle \Re(\Xi_s \cdot \mathcal{P}^{s}_{nn}(0)) \cdot [B_{\bar{s}}]_N(t)\rangle. \tag{61}$$

The initial conditions are sampled from the Metropolis algorithm with the distribution function in Eq. (55). The variables $\{R_\alpha, P_\alpha, \theta_\alpha, \varphi_\alpha\}$ are then propagated using the symplectic algorithm for NRPMD,[37] which separately updates the motion of the mapping variables and the ring polymer. The velocity Verlet algorithm is used to update the spin mapping variables based on Eq. (B2), with details provided in Appendix B. For s ≡ W, between 10^4 and 10^6 trajectories were run for four–six beads for the results presented hereafter, with a time step of 0.01 a.u. The NRPMD results presented for comparison require eight beads and up to 10^6 trajectories to converge. The MF-RPMD calculations require between four and five beads and 10^3 trajectories to converge.

TABLE II. Parameters for models I–VII.

Models	I	II	III	IV	V	VI	VII
Δ	10	4	1	1	1	0.1	0.1
ϵ	0	0	2	0.5	0	1.5	0
Beads	4	6	6	6	6	6	4

VI. RESULTS AND DISCUSSION

Figure 1 presents the nuclear probability distribution $P(R_0)$ (black solid curve) and the state-resolved nuclear probability distributions $P_1(R_0)$ (blue dashed curve) and $P_2(R_0)$ (red dashed curve) for a widely used model system described in Eq. (54). These distributions agree perfectly with the numerically exact results obtained from discrete variable representation (DVR) calculations.[69] The numerical convergence is achieved with only $N = 10$ beads. The SCS-partition function in Eq. (35) only requires two independent variables $\{\theta_\alpha, \varphi_\alpha\}$ for each bead, which is consistent with the number of electronic states, whereas the MMST-based partition functions, such as those used in the NRPMD or MV-RPMD methods require four independent variables. As the number of beads increases, the MMST-based approaches become numerically expensive. In addition, previous numerical investigations suggest that 16–32 beads are required to reach the same level of convergence with the MMST-based path-integral approaches.[46] This is likely due to the larger set of free variables to be sampled. Moreover, the general formalism of $\mathbf{\Gamma}_s$ in Eq. (38) does not explicitly require the evaluation of $\mathcal{M}_{nm}(R_\alpha) = \langle n|e^{-\beta_N \frac{1}{\hbar}\mathbf{H}_\alpha \cdot \hat{\mathbf{S}}}|m\rangle$ matrix, avoiding explicit diagonalization of the 2×2 matrix at a given R_α.

Figure 2 presents the nuclear position auto-correlation functions computed from SM-NRPMD (black solid lines), NRPMD[36,37] (green dashed lines), mean-field RPMD (MF-RPMD)[39,68] (blue dashed lines), and a numerically exact method (red dots). A brief description of the NRPMD and the mean-field RPMD approaches is provided in Appendix E. The SM-NRPMD calculations have been done with the index s = s̄ ≡ W (sampling with $\mathbf{\Gamma}_s \equiv \mathbf{\Gamma}_W$ and dynamics with $\tilde{H}_{\bar{s}} \equiv \tilde{H}_W$). In the adiabatic regime ($\beta\Delta \gg 1$) in panel (a), all methods agree perfectly with the exact result as expected. In the intermediate regime $\beta\Delta \approx 1$ in panel (b), all RPMD based approaches capture the correct oscillation frequency of the TCF, but they give different amplitudes that deviate from the exact

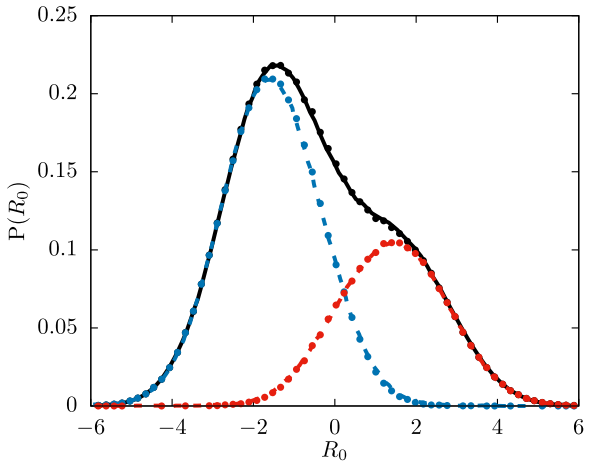

FIG. 1. Nuclear probability distribution (black solid curve) $P(R_0)$ of model 0 obtained from the SCS-partition function with $N = 10$ beads. The state specific distributions for state 1 (blue dashed curve) and state 2 (red dashed curve) are also shown. The results are compared with quantum exact calculations (filled circles).

Published under license by AIP Publishing

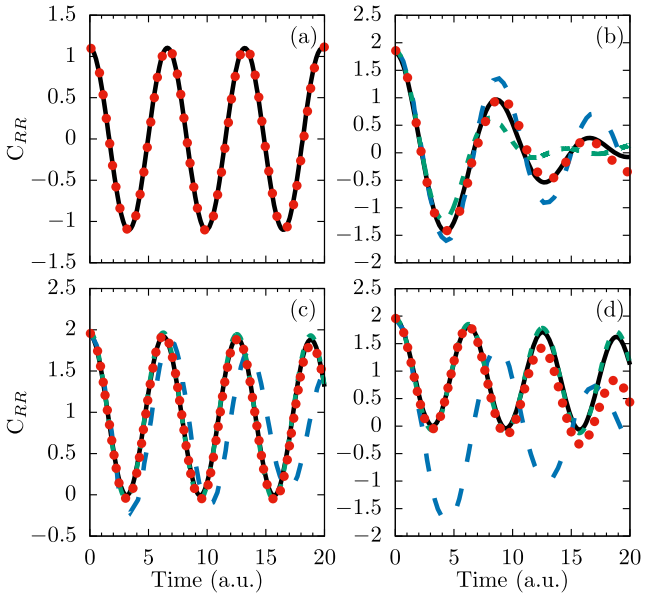

FIG. 2. Kubo-transformed nuclear position auto-correlation functions for (a) model I, (b) model V, (c) model VI, and (d) model VII. The results are obtained from SM-NRPMD with s ≡ W (black solid lines), MF-RPMD (blue dashed lines), and NRPMD[36] (green dashed lines), as well as numerically exact results (red dots).

result except the SM-NRPMD approach, which provides an excellent agreement with the exact TCF. In the non-adiabatic regime though $\beta\Delta \ll 1$ in panels (c) and (d), the MF-RPMD method cannot provide the correct amplitude nor oscillation frequency for the TCF. This is due to the fact that the MF-RPMD method does not have any explicit electronic state dynamics.[39,68] On the other hand, the results from both the SM-NRPMD and the NRPMD methods are in agreement with the exact results on all the range considered in panel (c) and at short time for panel (d). The non-adiabatic RPMD methods fail to capture the correct oscillation amplitude of $C_{RR}(t)$ at a longer time in panel (d), likely due to the Matsubara approximation[70] and the RPMD approximation,[71] from which the NRPMD dynamics is based upon.[45] The adiabatic potential of the model system considered here is $E_{\pm} = U_0(R) + \frac{1}{2}[V_1(R) + V_2(R)] \pm \sqrt{(V_1(R) - V_2(R))^2 + 4\Delta^2}$; hence, when $|\Delta| \gg |V_1(R) - V_2(R)|$ [the adiabatic limit in panel (a)], the ground adiabatic state is purely harmonic, and the dynamics is purely adiabatic (where the nuclear DOF stays on the ground adiabatic surface without any non-adiabatic transitions). Under this limit, the RPMD approach is known to be exact,[25] explaining the perfect agreement between all of the RPMD related methods and the exact results in the adiabatic case [Fig. 2(a)]. However, in the non-adiabatic case [Fig. 2(d)], $|\Delta| \ll |V_1(R) - V_2(R)|$, the adiabatic potential is far from the harmonic one, and there is a lot of non-adiabatic transitions among the two adiabatic surfaces; hence, the agreement between the exact result and the NRPMD TCF is not as perfect as the adiabatic case. Nonetheless, we notice that even in the most challenging highly non-adiabatic case, only four beads are required to converge the results. Again, for all cases investigated here, a smaller or an equal number of beads are required to converge the SM-NRPMD results compared to the TCF computed from the previous NRPMD approach based on the MMST mapping formalism.[36,41] We have also performed the SM-NRPMD simulations with (i) s ≡ Q sampling and dynamics obeying s̄ ≡ P and (ii) s ≡ P sampling and dynamics obeying s̄ ≡ Q. Additional results and discussions are provided in Appendix E.

Figure 3 presents the nuclear position and the state 1 electronic population auto-correlation functions computed from the SM-NRPMD (black solid lines) and NRPMD (green dashed lines) methods, as well as with a numerically exact approach (red dots) for models II, III, and V. Accurately describing electronic Rabi oscillations are essential for non-adiabatic dynamics simulations. Both the SM-NRPMD and the NRPMD results agree well with the exact results in the adiabatic regime for model II, presented in Fig. 3(a), and provide reasonably good results for the model systems in the intermediate regimes presented in Figs. 3(b) and 3(c). MV-RPMD,[39] on the other hand, cannot correctly capture the electronic oscillations in these population auto-correlation functions (results not

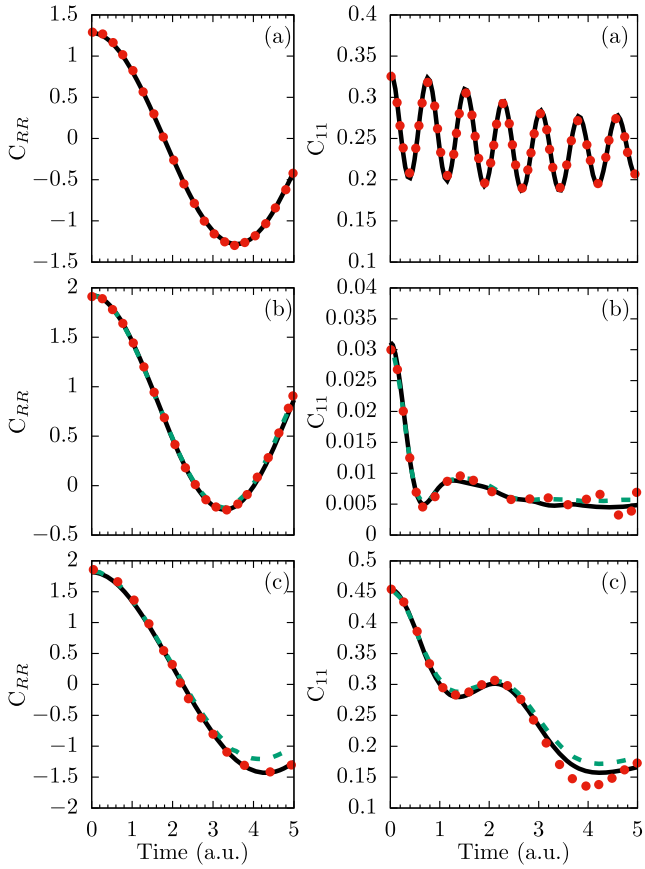

FIG. 3. Kubo-transformed nuclear position auto-correlation functions (left panels) and state 1 electronic population auto-correlation functions (right panels) for (a) model II, (b) model III, and (c) model V. The results are obtained from SM-NRPMD with s ≡ W (black solid lines) and NRPMD[36] (green dashed lines), compared to the numerically exact results (red dots).

Published under license by AIP Publishing

shown) due to the contamination of the true electronic Rabi oscillations with the inter-bead couplings in the mapping ring polymer Hamiltonian.[39] Note that the MMST formalism[47] as well as the NRPMD approach[45] indeed rigorously conserves the electronic Rabi oscillations for an isolated electronic subsystem. Based on the connection between the MMST formalism and the spin mapping formalism [Eq. (A4)], we expect that the latter should also rigorously conserve the electronic Rabi oscillations for an isolated electronic subsystem. The algebraic proof of this is subjected to future investigations.

Figure 4 presents the time-dependent expectation values of the nuclear position $\langle R\rangle$ [using $\hat{A} = \hat{\mathcal{I}} \otimes \hat{\mathbb{1}}_R$ and $\hat{B} = \hat{R}$ in $C^{\mathrm{K}}_{AB}(t)$] and the state 1 population $\langle \mathrm{P}_1\rangle$ (using $\hat{A} = \hat{\mathcal{I}} \otimes \hat{\mathbb{1}}_R$ and $\hat{B} = |1\rangle\langle 1|$) in model IV (a non-adiabatic case with bias). These expectation values are computed with both the SM-NRPMD (solid lines) and NRPMD (dashed lines) methods and are compared to the exact values. Because the system is under thermal equilibrium, these values should be conserved along the dynamics. As we can see in Fig. 4, by increasing the number of beads from $N = 2$ (magenta) to $N = 4$ (blue) and $N = 6$ (green), the SM-NRPMD method (with s ≡ W) almost provides time-independent expectation values. The MMST-based approaches, such as the NRPMD method[36,58] (dashed lines), cannot provide a constant expectation value with the same number of beads. We conjecture that for a large number of beads, SM-NRPMD (with s ≡ W) might preserve the initial quantum Boltzmann distribution (QBD). This conjecture is also corroborated by the numerical evidence that the initial distribution function $\mathrm{Tr}_{\mathrm{e}}[\mathbf{\Gamma}_{\mathrm{s}}] \cdot e^{-\beta_N \bar{H}_0(\mathbf{R})}$ [inside Eq. (35)] is conserved by the EOMs in Eqs. (53a)–(53c) at the single-trajectory level with a large number of beads ($N > 32$). On the other hand, we do not have a rigorous analytical proof that whether SM-NRPMD preserves QBD, and this is subject to further investigations. To summarize, with a finite number of beads, the SM-NRPMD (with s ≡ W) largely conserves the initial quantum Boltzmann distribution, providing an almost time-independent expectation value for systems under thermal equilibrium. This is a significant improvement compared to the MMST-based NRPMD dynamics.[36,37,58]

Compared to the previous NRPMD approach with the MMST formalism, the SM-NRPMD approach provides the additional advantage that the dynamics is invariant with respect to the splitting between the state-independent potential $U_0(\hat{R})$ and the state-dependent potential. This is because the spin mapping formalism explicitly enforces the total population to be 1 such that $[\hat{\mathcal{I}}]_{\mathrm{s}}(\mathbf{u}) = 1$. More explicitly, this can be seen in Eqs. (14a) and (14b), leading to $U_0 = (\frac{1}{2} + r_{\mathrm{s}} \cos\theta) \cdot U_0 + (\frac{1}{2} - r_{\mathrm{s}} \cos\theta) \cdot U_0$. The MMST formalism, on the other hand, does not guarantee this property when using approximate quantum dynamics, and a brief discussion between these two mapping approaches is provided in Appendix A. In order to explicitly demonstrate this advantage, we incorporate the state-independent quadratic term potential into the state-dependent Hamiltonian as follows:

$$\hat{H} = \frac{\hat{p}^2}{2m} + \begin{pmatrix} \frac{1}{2}m\omega^2\hat{R}^2 + \hat{R} + \epsilon & \Delta \\ \Delta & \frac{1}{2}m\omega^2\hat{R}^2 - \hat{R} - \epsilon \end{pmatrix}.$$

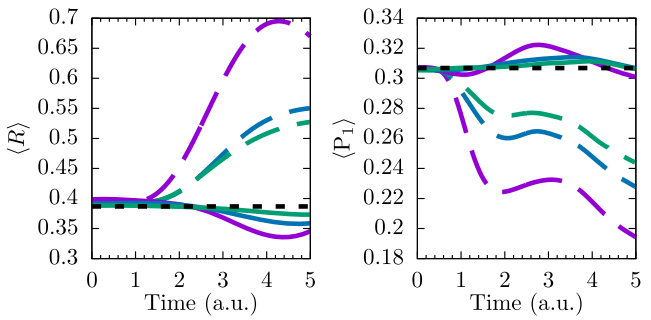

FIG. 4. Expectation values of the nuclear position operator (left panel) and the electronic population of state 1 (right panel) for model IV (intermediate regime). The results are obtained from SM-NRPMD with s ≡ W (solid lines) and NRPMD[36,58] (dashed lines) methods. The results for $N = 2$ (magenta lines), $N = 4$ (blue lines), and $N = 6$ (green lines) beads are shown.

Figure 5 presents the Kubo-transformed nuclear position and state 1 population auto-correlation functions for model V (non-adiabatic case) when including the quadratic potential $U_0(R)$ into the state-dependent part. The results are obtained with the NRPMD method[36] using the MMST formalism [panels (a)–(d)] and with the SM-NRPMD method using the spin mapping formalism [panels (e)–(h)]. When including U_0 into the state-dependent potential, the NRPMD dynamics becomes unstable and completely breaks down at $t \approx 3.5$ a.u., as some trajectories within the ensemble start to diverge, causing numerical instabilities. The nuclear position and state 1 population of three representative trajectories when including U_0 into the state-dependent potential are shown with dashed lines in Figs. 5(c) and 5(d), compared to the case where the quadratic term U_0 is treated as a state-independent potential (solid lines). When individual trajectories have a total population that deviates from 1 [as shown in Fig. 5(d)] in the MMST formalism, the total population also multiplies in front of U_0, resulting in an incorrect force acting on the nuclear DOF, as well as unstable motion. Due to this, including U_0 into the state-dependent Hamiltonian could be numerically challenging and eventually causes numerical instabilities. In addition, the results of the auto-correlation functions (before diverging) are different than those obtained in Figs. 2(b) and 3(c), indicating that different splitting of state-dependent and state-independent potential in the MMST formalism can lead to different numerical results when using approximate quantum dynamics approaches.[44]

Figures 5(e)–5(h) present the same comparisons using the SM-NRPMD method (with s ≡ W). As expected, the dynamics is invariant under different ways of partitioning $U_0(R)$. Figures 5(e) and 5(f) present the Kubo-transformed TCFs when including $U_0(R)$ in the state-dependent potential, providing identical results to those presented in Figs. 2(b) and 3(c). In fact, the dynamics is invariant at the single-trajectory level, as clearly indicated in Figs. 5(g) and 5(h). This is guaranteed because the total population is always bounded by 1 in spin mapping;[54] hence, the quadratic potential is always $(\frac{1}{2} + r_{\mathrm{s}} \cos\theta) \cdot U_0 + (\frac{1}{2} - r_{\mathrm{s}} \cos\theta) \cdot U_0 = U_0$. This is another unique numerical advantage of using the spin mapping formalism compared to the MMST mapping formalism, in addition to the better preservation of the initial quantum distribution demonstrated in Fig. 4.

Published under license by AIP Publishing

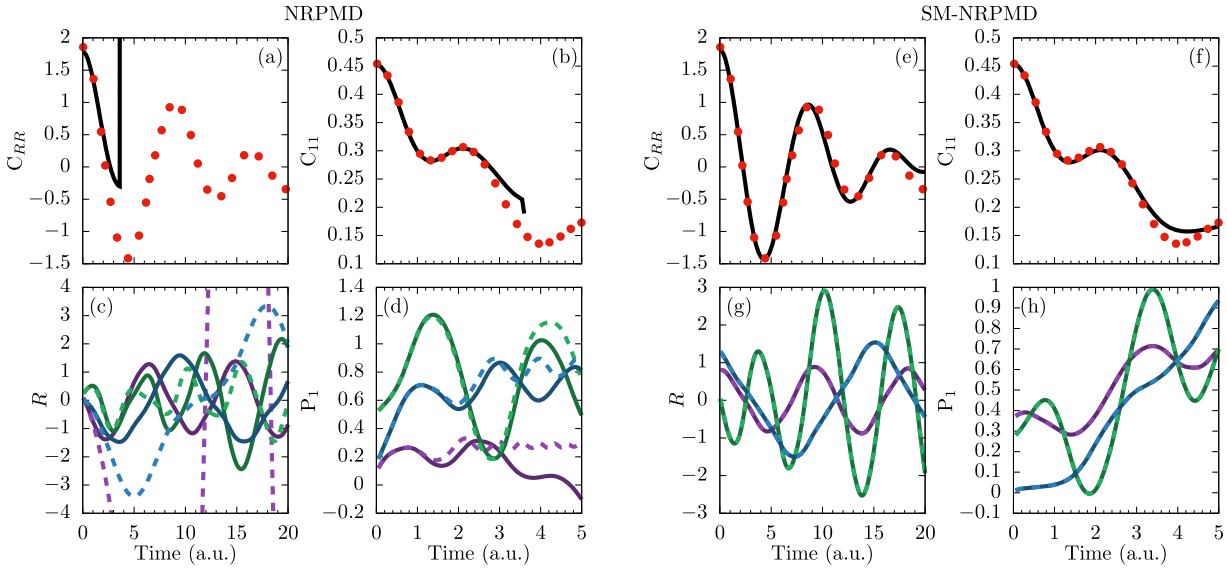

FIG. 5. The influence of including the quadratic potential $U_0(R)$ into the state-dependent Hamiltonian for model V. Left panels (a)–(d) present the results obtained from the NRPMD method[36] using the MMST mapping formalism. The Kubo-transformed position auto-correlation functions [panel (a)] and state 1 population auto-correlation functions [panel (b)] are computed with NRPMD (black lines) and exact approaches (red dots). Panels (c) and (d) present three representative trajectories (blue lines, magenta lines, and green lines) along which $\bar{R} = \frac{1}{N}\sum_{\alpha=1}^{N} R_\alpha$ [panel (c)] and $\bar{P}_1 = \frac{1}{N}\sum_{\alpha=1}^{N} \frac{1}{2}\left([q_\alpha]_1^2 + [p_\alpha]_1^2 - 1\right)$ are computed [see Eq. (E4) in Appendix E]. The dynamics is propagated using the NRPMD approach with $U_0(R)$ (dashed lines) and without $U_0(R)$ (solid lines) inside the state-dependent potential. Right panels (e)–(h) present the results obtained from the SM-NRPMD method using the spin mapping with s ≡ W. Panels (g) and (h) present three representative trajectories along which $\bar{R} = \frac{1}{N}\sum_{\alpha=1}^{N} R_\alpha(t)$ [panel (c)] and $\bar{P}_1 = \frac{1}{N}\sum_{\alpha=1}^{N} \frac{1}{2} + r_W \cdot \cos\theta_\alpha$ are computed using SM-NRPMD.

Note that in the SM approach, a negative population is still possible in the case of the $\tilde{H}_P$ and $\tilde{H}_W$ [see Fig. 5(h)], but the population is not directly involved in the potential related to U_0. This negative population at the single-trajectory level, as can be seen in Fig. 5(h) at $t = 2$ a.u. (green curve), is due to the fact that the trajectory is moving outside the range of $0 \le \frac{1}{2} + r_W \cos\theta_\alpha \le 1$. This problem is closely related to the mapping oscillator ZPE leakage problem[21] in the MMST formalism as the MMST ZPE is closely related to the Bloch sphere radius r_s as shown in Eq. (A5). In that sense, when the Bloch angle θ_α in the spin mapping formalism is moving into the negative population region, it corresponds to a situation where the total action in the MMST formalism becomes smaller than the mapping ZPE parameter.[53] On the other hand, the negative population will be a less severe problem when performing an ensemble average of trajectories, but the problem still persists,[54,56] even though it is significantly improved than the situation in the original MMST formalism.[56] In addition, we observed that the bead average in the SM-NRPMD formalism further improves the results when examining the population from individual trajectories as we increase the number of beads.

Recent theoretical investigations in the MMST formalism have focused on choosing different ZPE parameters [γ in Eq. (A5)] to improve the population dynamics.[16,21,72,73] Based on the connection between the MMST and the spin mapping formalism [Eqs. (A4) and (A5)], adjusting the ZPE parameter γ corresponds to adjusting the radius of the spin Bloch sphere r_s, so we envision that this can also be accomplished in the spin mapping formalism. This is subject to the future investigations.

In addition, during the dynamics, the spin mapping variables θ and φ are bounded on the Bloch sphere of radius r_s, as opposed to unbounded phase space variables (in the mapping oscillator phase space) in the MMST formalism (see Appendix A). Together, these advantages of the spin mapping variables make it a more accurate and convenient mapping representation for developing non-adiabatic dynamics methods,[54,58] and we extend it to the non-adiabatic RPMD dynamics in this work.

VII. CONCLUSION

In this paper, we present a new non-adiabatic RPMD method based on the recent development of a spin mapping (SM) formalism.[54] The basis of the spin mapping variables, the spin coherent states, is of the same dimensionality as the electronic Hilbert subspace of the original system. Hence, the SM approach presents numerical advantages compared to the original harmonic oscillator-based mapping approach,[43,44,49] especially when the approximate dynamics method is used. These include that the total population for a single trajectory is always equal to 1, the dynamics is invariant under different ways of partitioning the state-independent and state-dependent potentials, and projections back to the electronic subspace[46] are no longer necessary to compute physical observables.

Using the spin mapping representation, we derive a general quantum partition function for the coupled electronic–nuclear system, which we refer to as the Spin Coherent State (SCS) partition function. We test the performance of the SCS-partition function

Published under license by AIP Publishing

by computing state-dependent nuclear distributions in a two-level system coupled to a harmonic DOF. Our results suggest that the SCS-partition function provides the exact quantum results using $N = 10$ beads, requiring fewer beads compared to the MMST-based quantum partition functions.[36,39,41,46] Furthermore, the SCS-partition function provides an analytical expression of the matrix elements of the thermal Boltzmann operator [Eq. (37)], facilitating the Monte Carlo numerical simulations. Using the different choices of index s in the Stratonovich–Weyl transformation, we find that the $s \equiv Q$ approach requires the fewest MC configurations to converge, whereas the $s \equiv W$ approach requires ten times more than the $s \equiv Q$ approach, and the $s \equiv P$ approach requires 10^3 more configurations to converge for $N = 10$ beads (this ratio increases when increasing the number of beads). Compared to the MMST-based approaches, the $s \equiv W$ approach requires a similar amount of configurations and a fewer number of beads to converge compared to the original NRPMD[36,37] method or the CS-RPMD method.[41]

Using the properties of the Stratonovich–Weyl transformation, we further justify the spin mapping (SM)-NRPMD Hamiltonian, which can be viewed as the unified Hamiltonian of the spin mapping Hamiltonian and the ring polymer Hamiltonian. Based on this Hamiltonian, we propose the SM-NRPMD dynamics, where the initial sampling is governed by the SCS-partition function and the dynamics is governed by the SM-NRPMD Hamiltonian. Using the DOF of r_s and $r_{\bar{s}}$, we find that by choosing $\{s \equiv W, \bar{s} \equiv W\}$, the SM-NRPMD method provides accurate Kubo-transformed nuclear position auto-correlation functions compared to the exact results for model systems that exhibit a broad range of parameters, from the electronically adiabatic to the non-adiabatic regime. It can also provide accurate population auto-correlation functions with the correct electronic Rabi oscillation frequency, as shown in our numerical results. The accuracy of SM-NRPMD appears to be equivalent (with some slight improvements in certain cases) to the accuracy obtained from MMST-based non-adiabatic RPMD methods, such as NRPMD[36,37] or CS-RPMD,[41] with a similar number of beads required to converge the dynamics and a similar amount of trajectories required to converge the calculations.

From our numerical results, the SM-NRPMD method seems to almost preserve the initial quantum Boltzmann distribution by providing nearly time-independent expectation values of the nuclear position and electronic population. Note that this is a numerical observation and the analytical proof is still required in the future. The MMST-based RPMD approaches, on the other hand, fail to generate expectation values of an observable with a so small deviation with time for systems under thermal equilibrium. Moreover, the SM-NRPMD method provides stable and invariant results regardless of how to partition the state-independent and state-dependent potentials, whereas the dynamics of MMST-based NRPMD method is highly sensitive to the specific choice of splitting of the potentials.

To summarize, SM-NRPMD provides accurate electronic non-adiabatic dynamics with explicit nuclear quantization, with additional advantages compared to the original MMST-based approaches including a normalized total population along a single trajectory and the invariant dynamics under different ways of partitioning the Hamiltonian. Future directions include generalizing the current formalism to multi-electronic states[54] as well as rigorously deriving the SM-NRPMD approach through the recent development of the non-adiabatic Matsubara framework.[45]

ACKNOWLEDGMENTS

This work was supported by the National Science Foundation CAREER Award under Grant No. CHE-1845747. P.H. acknowledges support from a Cottrell Scholar Award (a program by Research Corporation for Science Advancement). Computing resources were provided by the Center for Integrated Research Computing (CIRC) at the University of Rochester.

APPENDIX A: CONNECTION BETWEEN THE SPIN MAPPING AND THE MMST MAPPING

The spin mapping Hamiltonian $H_s(\mathbf{u})$ in Eq. (15) can be transformed into the MMST mapping Hamiltonian. The connection between these two mapping formalisms has been extensively discussed in Ref. 53. Consider the following variable transformations between the spin mapping variables $\mathbf{u}$ and the MMST mapping variables $\mathbf{q} = \{q_1, q_2\}$ and $\mathbf{p} = \{p_1, p_2\}$:

$$2r_s u_x = q_1 q_2 + p_1 p_2, \tag{A1a}$$

$$2r_s u_y = q_1 p_2 - q_2 p_1, \tag{A1b}$$

$$2r_s u_z = \frac{1}{2}\left(q_1^2 + p_1^2 - q_2^2 - p_2^2\right). \tag{A1c}$$

Using the above transformations in $H_s(\mathbf{u})$ [Eq. (15)] leads to

$$H_s = \frac{P^2}{2m} + U_0 + \frac{1}{2}(V_1 + V_2) + \frac{1}{4}(V_1 - V_2)\cdot\left(q_1^2 + p_1^2 - q_2^2 - p_2^2\right) + \Delta(q_1 q_2 + p_1 p_2), \tag{A2}$$

which is the MMST Hamiltonian for Hamiltonian $\hat{H}$ in Eq. (2), with a form that separates the trace $\frac{1}{N}\mathrm{Tr}_e\,\hat{V}$ and the trace-less part $\hat{V} - \frac{1}{N}\mathrm{Tr}_e\,\hat{V}$, as recommended in the MMST literature.[14,74]

Using $|\mathbf{u}|^2 = \sin^2\theta\cos^2\varphi + \sin^2\theta\sin^2\varphi + \cos^2\theta = 1$ and Eq. (A1), one can show that

$$4r_s = q_1^2 + q_2^2 + p_1^2 + p_2^2, \tag{A3}$$

which is often referred to as the total action of the mapping variables.[7] It is also a conserved quantity of the MMST Hamiltonian in Eq. (A2). Using this property, one can rewrite the MMST Hamiltonian in Eq. (A2) as follows:

$$\begin{aligned} H_s &= \frac{P^2}{2m} + U_0 + \Delta(q_1 q_2 + p_1 p_2) \\ &\quad + \frac{1}{2}V_1\cdot\left(\frac{q_1^2 + p_1^2 - q_2^2 - p_2^2}{2} + 1 + 2r_s - 2r_s\right) \\ &\quad + \frac{1}{2}V_2\cdot\left(\frac{q_2^2 + p_2^2 - q_1^2 - p_1^2}{2} + 1 + 2r_s - 2r_s\right) \\ &= \frac{P^2}{2m} + U_0 + \Delta(q_1 q_2 + p_1 p_2) + \frac{1}{2}\sum_{n=1}^{2} V_n\cdot(q_n^2 + p_n^2 - \gamma), \end{aligned} \tag{A4}$$

Published under license by AIP Publishing

where the MMST mapping oscillators' zero-point energy correction is defined as

$$\gamma = 2r_s - 1. \tag{A5}$$

Connecting to the spin mapping Hamiltonian, we can hence identify H_Q as MMST formalism with $\gamma = 0$, H_P as $\gamma = 2$, and H_W as $\gamma = \sqrt{3} - 1$ [which is the recommended value in the symmetric quasi-classical (SQC) approach[74] that was derived based on analogy with spin].

Note that the MMST Hamiltonian in Eq. (A4) has been historically introduced through the mapping relation $|i\rangle\langle j| \to a_i^\dagger \hat{a}_j = \frac{1}{\sqrt{2}}(\hat{q}_i - i\hat{p}_i) \cdot \frac{1}{\sqrt{2}}(\hat{q}_j + \hat{p}_j)$, as well as using $[p_i, q_i] = i$ (or effectively, $[p_i, q_i] = i\gamma$ for the adjusted mapping oscillator ZPE); hence,

$$\sum_{ij} V_{ij}(\hat{R})|i\rangle\langle j| \to \sum_{ij} V_{ij} a_i^\dagger \hat{a}_j = \frac{1}{2}\sum_{ij} V_{ij}(\hat{R})(\hat{q}_i\hat{q}_j + \hat{p}_i\hat{p}_j - \gamma\delta_{ij}). \tag{A6}$$

The fundamental differences between the spin mapping Hamiltonian in Eq. (2) and the MMST Hamiltonian in Eq. (A4) are the following: (i) for a two-state system, the spin mapping Hamiltonian only has two independent variables θ and φ, thus the same dimensionality of the original electronic subspace, whereas the MMST Hamiltonian has effectively four independent variables $\{p_1, q_1, p_2, q_2\}$, hence a larger dimensionality. (ii) The total population of the spin mapping is always 1, whereas this is not always guaranteed in the MMST mapping formalism.[53]

APPENDIX B: EQUATIONS OF MOTION FOR θ AND φ

Equation (17) can also be equivalently expressed as EOMs in θ and φ. Using $\dot{u}_z = -\dot{\theta}\sin\theta = H_x u_y - H_y u_x$ as well as $\dot{u}_x = \dot{\theta}\cos\theta\cos\varphi - \dot{\varphi}\sin\theta\sin\varphi = H_y u_z - H_z u_y$, we can derive the following equations:

$$\dot{\theta} = \frac{1}{\hbar}(-H_x \sin\varphi + H_y \cos\varphi), \tag{B1a}$$

$$\dot{\varphi} = \frac{1}{\hbar}\left(H_z - H_x\frac{\cos\varphi}{\tan\theta} - H_y\frac{\sin\varphi}{\tan\theta}\right). \tag{B1b}$$

It is interesting to note that the above equations are equivalent to the following:

$$\dot{\theta} = \frac{1}{r_s\sin\theta}\frac{\partial H_s(\mathbf{u})}{\partial\varphi}, \tag{B2a}$$

$$\dot{\varphi} = -\frac{1}{r_s\sin\theta}\frac{\partial H_s(\mathbf{u})}{\partial\theta}, \tag{B2b}$$

from which we obtain the conjugate variables $\dot{\varphi}$ and $r_s\cos\theta$ related to the spin mapping representation, where the latter plays the role of conjugate momentum[48] to φ as

$$\frac{d}{dt}(r_s\cos\theta) = -\frac{\partial H_s(\mathbf{u})}{\partial\varphi}, \tag{B3a}$$

$$\dot{\varphi} = \frac{\partial H_s(\mathbf{u})}{\partial(r_s\cos\theta)}. \tag{B3b}$$

The relationship between the Hamiltonian $H_s(\mathbf{u})$ and the Lagrangian is $H(\theta,\varphi) = \dot{\varphi}\cdot(r_s\cos\theta) - \mathcal{L}(\varphi,\dot{\varphi})$.

Note that under the non-equilibrium condition with a focused initial condition, such as $[|1\rangle\langle 1|]_s(\mathbf{u}) = \frac{1}{2} + r_s\cos\theta = 1$ [Eq. (14a)], it requires $\cos\theta = 1$ under s ≡ Q, which makes the above EOMs ill-defined in terms of $1/\sin\theta$ and $1/\tan\theta$. Thus, $\mathbf{u}$ is a more convenient dynamical variable than $\{\theta,\phi\}$ for this scenario. Under the thermal equilibrium condition (such as examples in this paper), the system will never reach $\theta = 0$, and we find that using Eq. (B2) is numerically more convenient. We hence use the velocity Verlet algorithm to evolve θ and φ, which avoids the necessity to compute any derivative of the potential, as is the case for $\dot{\mathbf{u}}$.

Using the fact that $\{\varphi, r_s\cos\theta\}$ are the canonical variables of the Hamiltonian H_s, we use the velocity Verlet algorithm to propagate the equation of motion, with (i) a half time step of the "momentum" $r_s\cos\theta$ (or θ as evolving the former is equivalent to the latter using the chain rule), (ii) then followed by a full time step of the "position" φ, and (iii) finally, the second half time step to propagate $r_s\cos\theta$. Note that a more stable propagation scheme of the MMST mapping variables is available,[14,75] which rigorously guarantees the symplectic propagation. Based on the connection between the spin mapping formalism and the MMST mapping formalism, one should be able to use these algorithms for the spin variable propagation.

APPENDIX C: ELEMENTARY RELATIONS IN SPIN MAPPING REPRESENTATION

Here, we verify several basic properties of the Stratonovich–Weyl transforms. We begin by explicitly expressing $\hat{w}_s$ as follows:

$$\hat{w}_s(\mathbf{u}) = \begin{pmatrix} \frac{1}{2} + r_s\cos\theta & r_s\sin\theta\cdot e^{-i\varphi} \\ r_s\sin\theta\cdot e^{i\varphi} & \frac{1}{2} - r_s\cos\theta \end{pmatrix} \equiv \begin{pmatrix} w_{11}^s & w_{12}^s \\ w_{21}^s & w_{22}^s \end{pmatrix}.$$

First, we verify that $\int d\mathbf{u} A_s(\mathbf{u}) = \mathrm{Tr}_e[\hat{A}]$ by computing $\mathrm{Tr}_e[\hat{A}]$ for a general operator $\hat{A}$ as follows:

$$\begin{aligned}\int d\mathbf{u} A_s(\mathbf{u}) &= \frac{1}{2\pi}\int_0^{2\pi} d\varphi \int_0^{\pi} d\theta \sin\theta\, \mathrm{Tr}_e[\hat{A}\hat{w}_s] \\ &= \frac{1}{2\pi}\int_0^{2\pi} d\varphi \int_0^{\pi} d\theta \sin\theta \Big(A_{11}\Big(\frac{1}{2} + r_s\cos\theta\Big) \\ &\quad + A_{12}r_s(\sin\theta\cos\varphi + i\sin\theta\sin\varphi) \\ &\quad + A_{21}r_s(\sin\theta\cos\varphi - i\sin\theta\sin\varphi) \\ &\quad + A_{22}\Big(\frac{1}{2} - r_s\cos\theta\Big)\Big) \\ &= A_{11} + A_{22} = \mathrm{Tr}_e[\hat{A}],\end{aligned} \tag{C1}$$

where we have used the elementary results of integrals $\int_0^\pi d\theta \sin\theta = 2$, $\int_0^\pi d\theta \cos\theta\sin\theta = 0$, $\int_0^{2\pi} d\varphi\cos\varphi = 0$, and $\int_0^{2\pi} d\varphi \sin\varphi = 0$. Using these integrals, it is also straightforward to verify that

$$\int d\mathbf{u}\hat{w}_s(\mathbf{u}) = \frac{1}{2\pi}\int_0^{2\pi} d\varphi \int_0^{\pi} d\theta \sin\theta\Big(\frac{1}{2}\hat{\mathcal{I}} + r_s\mathbf{u}\cdot\hat{\boldsymbol{\sigma}}\Big) = \hat{\mathcal{I}}, \tag{C2}$$

proving the resolution of identity in the spin mapping coherent state basis.

Published under license by AIP Publishing

For the Stratonovich–Weyl transform of the product of two operators $\hat{A}$ and $\hat{B}$, one can show that

$$\begin{aligned}\int \mathrm{d}\mathbf{u} A_{\mathrm{s}} B_{\bar{\mathrm{s}}}(\mathbf{u}) &= \int \mathrm{d}\mathbf{u}\, \mathrm{Tr}_{\mathrm{e}}\left[\hat{A}\hat{w}_{\mathrm{s}}\right]\mathrm{Tr}_{\mathrm{e}}\left[\hat{B}\hat{w}_{\bar{\mathrm{s}}}\right] \\ &= \int \mathrm{d}\mathbf{u}\left(A_{11}w^{\mathrm{s}}_{11} + A_{12}w^{\mathrm{s}}_{21} + A_{21}w^{\mathrm{s}}_{12} + A_{22}w^{\mathrm{s}}_{22}\right) \\ &\quad \cdot \left(B_{11}w^{\bar{\mathrm{s}}}_{11} + B_{12}w^{\bar{\mathrm{s}}}_{21} + B_{21}w^{\bar{\mathrm{s}}}_{12} + B_{22}w^{\bar{\mathrm{s}}}_{22}\right). \end{aligned} \tag{C3}$$

Note that any of the above terms that contains $\int_0^{2\pi} d\varphi e^{\pm i\varphi}$ or $\int_0^{2\pi} d\varphi e^{\pm 2i\varphi}$ will be zero. Hence, only the terms without $e^{\pm i\varphi}$ survive. They are either $w^{\mathrm{s}}_{11}w^{\bar{\mathrm{s}}}_{11}$, $w^{\mathrm{s}}_{22}w^{\bar{\mathrm{s}}}_{22}$, or $w^{\mathrm{s}}_{12}w^{\bar{\mathrm{s}}}_{21}$, $w^{\mathrm{s}}_{21}w^{\bar{\mathrm{s}}}_{12}$. For the term related to $A_{11}B_{11}\cdot\int \mathrm{d}\mathbf{u} w^{\mathrm{s}}_{11}w^{\bar{\mathrm{s}}}_{11}$, the integral related to the mapping variables is

$$\int \mathrm{d}\mathbf{u} w^{\mathrm{s}}_{11}w^{\bar{\mathrm{s}}}_{11} = \int_0^{\pi} \mathrm{d}\theta \sin\theta\left(\frac{1}{2} + r_{\mathrm{s}}\cos\theta\right)\left(\frac{1}{2} + r_{\bar{\mathrm{s}}}\cos\theta\right) = 1,$$

where we used the fact that $r_{\mathrm{s}}\cdot r_{\bar{\mathrm{s}}} = 3/4$, $\int_0^{\pi}\mathrm{d}\theta\sin\theta = 2$, and $\int_0^{\pi}\mathrm{d}\theta\sin\theta\cos^2\theta = \frac{2}{3}$. Similarly, one can show that $\int \mathrm{d}\mathbf{u} w^{\mathrm{s}}_{22}w^{\bar{\mathrm{s}}}_{22} = 1$ as well. The other non-zero terms are $A_{12}B_{21}\cdot\int \mathrm{d}\mathbf{u} w^{\mathrm{s}}_{21}w^{\bar{\mathrm{s}}}_{12}$ and $A_{21}B_{12}\cdot\int \mathrm{d}\mathbf{u} w^{\mathrm{s}}_{12}w^{\bar{\mathrm{s}}}_{21}$, with the weighting factor

$$\int \mathrm{d}\mathbf{u} w^{\mathrm{s}}_{21}w^{\bar{\mathrm{s}}}_{12} = \int \mathrm{d}\mathbf{u} w^{\mathrm{s}}_{12}w^{\bar{\mathrm{s}}}_{21} = \int_0^{\pi}\mathrm{d}\theta \sin\theta\cdot r_{\mathrm{s}}r_{\bar{\mathrm{s}}}\cdot\sin^2\theta = 1,$$

where $\int_0^{\pi}\mathrm{d}\theta\sin^3\theta = 4/3$. Putting all these results together, we have

$$\begin{aligned}\int \mathrm{d}\mathbf{u} A_{\mathrm{s}} B_{\bar{\mathrm{s}}}(\mathbf{u}) &= A_{11}B_{11} + A_{12}B_{21} + A_{21}B_{12} + A_{22}B_{22} \\ &= \mathrm{Tr}_{\mathrm{e}}[\hat{A}\hat{B}], \end{aligned} \tag{C4}$$

which is Eq. (21) of the main text.

APPENDIX D: DERIVATION OF THE SCS-PARTITION FUNCTION

We derive an analytic expression of the Boltzmann operator in the spin mapping representation. For that, we first Taylor expand it as

$$e^{-\beta_N\frac{1}{\hbar}\mathbf{H}_\alpha\cdot\hat{\mathbf{S}}} = \hat{\mathcal{I}} - \beta_N\frac{1}{\hbar}\mathbf{H}_\alpha\cdot\hat{\mathbf{S}} + \frac{\beta_N^2}{2!}\left(\frac{1}{\hbar}\mathbf{H}_\alpha\cdot\hat{\mathbf{S}}\right)^2 - \frac{\beta_N^3}{3!}\left(\frac{1}{\hbar}\mathbf{H}_\alpha\cdot\hat{\mathbf{S}}\right)^3 + \cdots, \tag{D1}$$

where we explicitly keep all terms. Using the fact that $(\frac{1}{\hbar}\mathbf{H}_\alpha\cdot\hat{\mathbf{S}})^2 = |\mathbf{H}_\alpha|^2/4\times\hat{\mathcal{I}}$, Eq. (D1) leads to an expression with two different types of terms that can be identified as Taylor expansions of hyperbolic cosine and hyperbolic sine as follows:

$$\begin{aligned} e^{-\beta_N\frac{1}{\hbar}\mathbf{H}_\alpha\cdot\hat{\mathbf{S}}} &= \sum_{j=0}^{\infty}\frac{1}{(2j)!}\left(\beta_N\frac{|\mathbf{H}_\alpha|}{2}\right)^{2j}\hat{\mathcal{I}} - \frac{2\mathbf{H}_\alpha\cdot\hat{\mathbf{S}}}{\hbar|\mathbf{H}_\alpha|} \\ &\quad\times\sum_{j=0}^{\infty}\frac{1}{(2j+1)!}\left(\beta_N\frac{|\mathbf{H}(R_\alpha)|}{2}\right)^{2j+1} \\ &= \cosh\frac{\beta_N|\mathbf{H}_\alpha|}{2}\hat{\mathcal{I}} - \frac{\mathbf{H}_\alpha\cdot\hat{\boldsymbol{\sigma}}}{|\mathbf{H}_\alpha|}\sinh\frac{\beta_N|\mathbf{H}_\alpha|}{2}. \end{aligned} \tag{D2}$$

Using the above result as well as the identity $(\mathbf{A}\cdot\hat{\boldsymbol{\sigma}})(\mathbf{B}\cdot\hat{\boldsymbol{\sigma}}) = \mathbf{A}\cdot\mathbf{B}\hat{\mathcal{I}} + i\mathbf{A}\times\mathbf{B}\cdot\hat{\boldsymbol{\sigma}}$, one can show that

$$\begin{aligned} e^{-\beta_N\frac{1}{\hbar}\mathbf{H}_\alpha\cdot\hat{\mathbf{S}}}\hat{w}_{\mathrm{s}}(\mathbf{u}_\alpha) &= \cosh\left(\frac{\beta_N|\mathbf{H}_\alpha|}{2}\right)\left(\frac{1}{2}\hat{\mathcal{I}} + r_{\mathrm{s}}\mathbf{u}_\alpha\cdot\hat{\boldsymbol{\sigma}}\right) \\ &\quad - \frac{1}{|\mathbf{H}_\alpha|}\sinh\left(\frac{\beta_N|\mathbf{H}_\alpha|}{2}\right) \\ &\quad\times\left(\frac{1}{2}\mathbf{H}_\alpha\cdot\hat{\boldsymbol{\sigma}} + r_{\mathrm{s}}\left(\mathbf{H}_\alpha\cdot\mathbf{u}_\alpha\hat{\mathcal{I}} + i\mathbf{H}_\alpha\times\mathbf{u}_\alpha\cdot\hat{\boldsymbol{\sigma}}\right)\right) \\ &= \left(\frac{1}{2}\cosh\frac{\beta_N|\mathbf{H}_\alpha|}{2} - r_{\mathrm{s}}\frac{\mathbf{H}_\alpha}{|\mathbf{H}_\alpha|}\cdot\mathbf{u}_\alpha\sinh\frac{\beta_N|\mathbf{H}_\alpha|}{2}\right)\hat{\mathcal{I}} \\ &\quad + \left(r_{\mathrm{s}}\mathbf{u}_\alpha\cosh\frac{\beta_N|\mathbf{H}_\alpha|}{2} - \frac{1}{|\mathbf{H}_\alpha|}\left(\frac{\mathbf{H}_\alpha}{2} + ir_{\mathrm{s}}\mathbf{H}_\alpha\times\mathbf{u}_\alpha\right)\right. \\ &\quad\left.\times\sinh\frac{\beta_N|\mathbf{H}_\alpha|}{2}\right)\cdot\hat{\boldsymbol{\sigma}}. \end{aligned} \tag{D3}$$

This is the general expression of $\boldsymbol{\Gamma}_{\mathrm{s}}$ in the SCS-partition function [Eq. (35)] for any SW transformation.

APPENDIX E: NRPMD AND MEAN-FIELD-RPMD

The NRPMD method[36] was first proposed by Thoss and Richardson as a model dynamics. Recently, it was rigorously derived from the non-adiabatic Matsubara dynamics formalism.[45] It uses the MMST formalism [Eq. (A6)] to describe the electronic DOFs and the ring polymer path-integral formalism to describe the nuclear DOFs. When operators $\hat{A}$ and $\hat{B}$ are both functions of $\hat{R}$, the NRPMD TCF is expressed as

$$\begin{aligned} C_{AB}(t) &= \frac{1}{\mathcal{Z}}\lim_{N\to\infty}\int \mathrm{d}\{R_\alpha\}\int \mathrm{d}\{P_\alpha\}\int \mathrm{d}\{\mathbf{q}_\alpha\}\int \mathrm{d}\{\mathbf{p}_\alpha\} \\ &\quad\times \mathrm{Tr}_{\mathrm{e}}[\boldsymbol{\Gamma}'(\mathbf{R},\mathbf{q},\mathbf{p})]e^{-\beta_N H_{\mathrm{rp}}(\mathbf{R})}\bar{A}(\mathbf{R})\bar{B}(\mathbf{R}_t), \end{aligned} \tag{E1}$$

where $H_{\mathrm{rp}}(\mathbf{R}) = \sum_{\alpha=1}^{N}\frac{P_\alpha^2}{2m} + \frac{m}{2\beta_N^2\hbar^2}(R_\alpha - R_{\alpha-1})^2 + U_0(R_\alpha)$ corresponds to the ring polymer Hamiltonian with the state-independent potential, $\bar{A}(\mathbf{R}) = \frac{1}{N}\sum_{\alpha=1}^{N}A(R_\alpha)$ and $\bar{B}(\mathbf{R}_t) = \frac{1}{N}\sum_{\alpha=1}^{N}B(R_\alpha(t))$, and $\boldsymbol{\Gamma}'(\mathbf{R},\mathbf{q},\mathbf{p})$ is expressed as[36]

$$\boldsymbol{\Gamma}'(\mathbf{R},\mathbf{q},\mathbf{p}) = e^{-\mathcal{G}_N}\prod_{\alpha=1}^{N}\left[\boldsymbol{\mathcal{M}}'(R_\alpha)\mathbf{q}_\alpha\mathbf{q}_\alpha^{\mathrm{T}}\boldsymbol{\mathcal{M}}'(R_\alpha)\mathbf{p}_\alpha\mathbf{p}_\alpha^{\mathrm{T}}\right],$$

with $\mathcal{G}_N = \sum_{\alpha=1}^{N}(\mathbf{q}_\alpha^{\mathrm{T}}\mathbf{q}_\alpha + \mathbf{p}_\alpha^{\mathrm{T}}\mathbf{p}_\alpha)$ and $\mathcal{M}'_{ij}(R_\alpha) = \langle i|e^{-\frac{1}{2}\beta_N\hat{V}_{\mathrm{e}}(R_\alpha)}|j\rangle$. Note that $\mathrm{Tr}_{\mathrm{e}}[\boldsymbol{\Gamma}'(\mathbf{R},\mathbf{q},\mathbf{p})]$ can also be equivalently expressed as $\mathrm{Tr}_{\mathrm{e}}[\boldsymbol{\Gamma}'(\mathbf{R},\mathbf{q},\mathbf{p})] = e^{-\mathcal{G}_N}\prod_{\alpha=1}^{N}[\mathbf{p}_{\alpha-1}^{\mathrm{T}}\boldsymbol{\mathcal{M}}'(R_\alpha)\mathbf{q}_\alpha]\cdot[\mathbf{q}_\alpha^{\mathrm{T}}\boldsymbol{\mathcal{M}}'(R_\alpha)\mathbf{p}_\alpha]$.

The dynamics is governed by the following NRPMD Hamiltonian:[36]

$$\begin{aligned} H_N &= \frac{1}{N}\sum_{\alpha=1}^{N}\left[\frac{P_\alpha^2}{2m} + \frac{m}{2\beta_N^2\hbar^2}(R_\alpha - R_{\alpha-1})^2 + U_0(R_\alpha)\right. \\ &\quad\left. + \frac{1}{2}\sum_{i,j=1}^{\mathcal{K}}V_{ij}(R_\alpha)\left([\mathbf{p}_\alpha]_i[\mathbf{p}_\alpha]_j + [\mathbf{q}_\alpha]_i[\mathbf{q}_\alpha]_j - \delta_{ij}\right)\right]. \end{aligned} \tag{E2}$$

The NRPMD Hamiltonian was derived from both the partition function expression[38] and a quantum Liouvillian.[45] It is closely

Published under license by AIP Publishing

related to the SM-NRPMD Hamiltonian in Eq. (45) through the transformations in Eq. (A1a).

When $\hat{A} = |i\rangle\langle i|$ and $\hat{B} = |j\rangle\langle j|$, the NRPMD TCF is

$$C_{AB}(t) = \frac{1}{\mathcal{Z}} \lim_{N\to\infty} \int \mathrm{d}\{R_\alpha\} \int \mathrm{d}\{P_\alpha\} \int \mathrm{d}\{\mathbf{q}_\alpha\} \int \mathrm{d}\{\mathbf{p}_\alpha\} \times \mathrm{Tr}_\mathrm{e}[\mathbf{\Gamma}'|i\rangle\langle i|] e^{-\beta_N H_\mathrm{rp}(\mathbf{R})} [\hat{a}_j^\dagger \hat{a}_j]_N(t), \tag{E3}$$

with the electronic state estimator[36,37]

$$P_j(t) = [\hat{a}_j^\dagger \hat{a}_j]_N = \frac{1}{N} \sum_{\alpha=1}^{N} \frac{1}{2} \left([\mathbf{q}_\alpha]_j^2 + [\mathbf{p}_\alpha]_j^2 - 1 \right). \tag{E4}$$

The mean-field (MF)-RPMD approach[68] can be viewed as a special limit of the NRPMD TCF [Eq. (E1)] by analytically integrating out the mapping variables in Eq. (E1) at $t = 0$. The MF-RPMD TCF[39,68] is

$$C_{AB}^\mathrm{MF}(t) = \frac{1}{\mathcal{Z}} \lim_{N\to\infty} \int \mathrm{d}\{R_\alpha\} \int \mathrm{d}\{P_\alpha\} \mathrm{Tr}_\mathrm{e}[\mathbf{\Gamma}''(\mathbf{R})] e^{-\beta_N H_\mathrm{rp}} \bar{A}(\mathbf{R}) \bar{B}(\mathbf{R}_t), \tag{E5}$$

where $\mathbf{\Gamma}''(\mathbf{R}) = \prod_{\alpha=1}^{N} \boldsymbol{\mathcal{M}}(R_\alpha)$ and $\mathcal{M}_{ij}(R_\alpha) = \langle i|e^{-\beta_N \hat{V}_\mathrm{e}(R_\alpha)}|j\rangle$. The MF-RPMD dynamics is governed by the MF-RPMD effective Hamiltonian[39,68] $H_\mathrm{MF} = H_\mathrm{rp} - \frac{1}{\beta} \ln|\mathrm{Tr}_\mathrm{e}[\mathbf{\Gamma}''(\mathbf{R})]|$. Note that MF-RPMD is not a new method and has been derived without using the mapping representation.[68]

APPENDIX F: ADDITIONAL RESULTS OF SM-NRPMD

In this section, we explore other possible choices of $\{\mathrm{s}, \bar{\mathrm{s}}\}$ in the SM-NRPMD dynamics. Using the model systems, we find that the $\{\mathrm{s} \equiv \mathrm{Q}, \bar{\mathrm{s}} \equiv \mathrm{P}\}$ choice provides the most efficient initial sampling, which requires ten times smaller configurations (trajectories) than the $\{\mathrm{s} \equiv \mathrm{W}, \bar{\mathrm{s}} \equiv \mathrm{W}\}$ choice when using $N = 6$ beads for a converged dynamics (due to a more severe sign problem). Thus, for pure quantum statistical quantities, $\{\mathrm{s} \equiv \mathrm{Q}\}$ provides the most efficient sampling. The TCF dynamics, unfortunately, seems to require more beads to converge. For correlation function calculations, this disadvantage counterbalances its advantage and makes the $\{\mathrm{s} \equiv \mathrm{W}, \bar{\mathrm{s}} \equiv \mathrm{W}\}$ more favorable.

The choice of $\{\mathrm{s} \equiv \mathrm{P}, \bar{\mathrm{s}} \equiv \mathrm{Q}\}$, on the other hand, provides a more accurate electronic auto-correlation function at a longer time. This finding agrees with the out of equilibrium calculations, which conclude that the $\bar{\mathrm{s}} \equiv \mathrm{Q}$ choice in the mapping Hamiltonian provides the most accurate electronic dynamics.[53] For the thermal TCF calculations, however, the initial sampling with the choice of $\mathrm{s} \equiv \mathrm{P}$ typically requires 10–10^2 more configurations to achieve a numerical convergence.

Figure 6 presents the SM-NRPMD position and state 1 population auto-correlation functions for models II, III, and V with the choice of $\{\mathrm{s} \equiv \mathrm{Q}, \bar{\mathrm{s}} \equiv \mathrm{P}\}$ (green solid lines) and $\{\mathrm{s} \equiv \mathrm{P}, \bar{\mathrm{s}} \equiv \mathrm{Q}\}$ (black solid lines), compared to the numerically exact results (red dots). Indeed, the $\mathrm{s} \equiv \mathrm{P}$ choice, hence $\bar{\mathrm{s}} \equiv \mathrm{Q}$ for the SM-NRPMD Hamiltonian, provides the most accurate electronic dynamics (more accurate than the $\{\mathrm{s} \equiv \mathrm{W}, \bar{\mathrm{s}} \equiv \mathrm{W}\}$ results in Fig. 3), with the price of using more trajectories to achieve numerical convergence of the TCF.

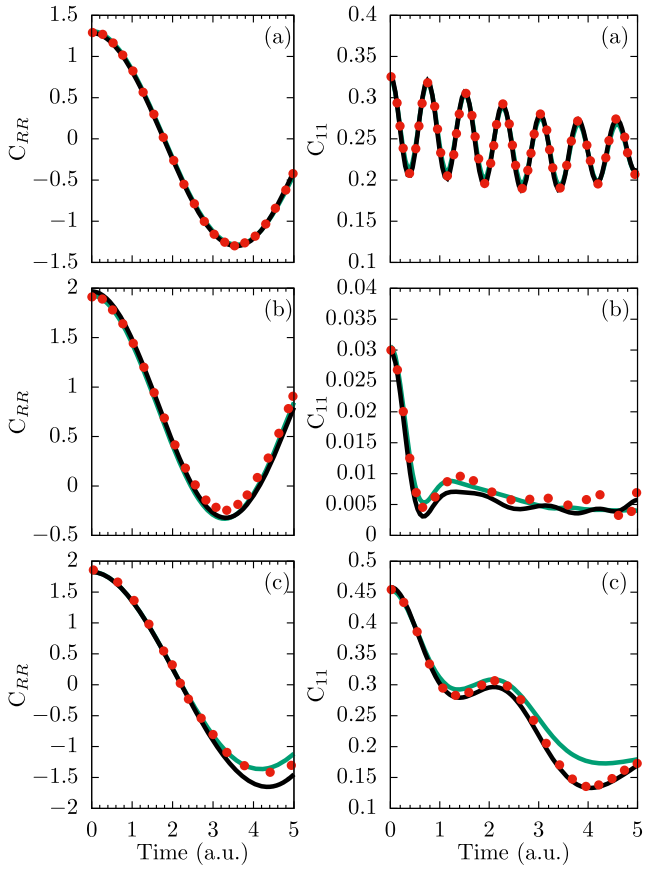

FIG. 6. Position auto-correlation functions (left panels) and their corresponding state 1 population auto-correlation functions (right panels) with $\mathrm{s} \equiv \mathrm{P}$ in black solid lines of models II (four beads), III (six beads), and V (four beads), respectively, in panels (a)–(c). Similar calculations with $\mathrm{s} \equiv \mathrm{Q}$ are presented in green solid lines for models II (eight beads), III (18 beads), and V (18 beads). The SM-NRPMD results are compared to the exact results (red dots).

The $\{\mathrm{s} \equiv \mathrm{Q}, \bar{\mathrm{s}} \equiv \mathrm{P}\}$ calculations (green lines) show a generally good agreement with the exact results but require more beads to converge (with up to 18 beads in the model calculations presented here). Calculations with such a large number of beads are made possible by the fast convergence of $\mathrm{s} \equiv \mathrm{Q}$ sampling (with 10^6 configurations for $N = 18$ beads).

Figure 7 presents the expectation values of the nuclear position operator and the state 1 electronic population for $\{\mathrm{s} \equiv \mathrm{Q}, \bar{\mathrm{s}} \equiv \mathrm{P}\}$ (solid lines) and $\{\mathrm{s} \equiv \mathrm{P}, \bar{\mathrm{s}} \equiv \mathrm{Q}\}$ (dashed lines). Both choices fail to provide the nearly time-independent expectation values that the choice of $\{\mathrm{s} \equiv \mathrm{W}, \bar{\mathrm{s}} \equiv \mathrm{W}\}$ can provide in Fig. 4. It also seems that both $\{\mathrm{s} \equiv \mathrm{Q}, \bar{\mathrm{s}} \equiv \mathrm{P}\}$ and $\{\mathrm{s} \equiv \mathrm{P}, \bar{\mathrm{s}} \equiv \mathrm{Q}\}$ require even more beads to converge these expectation values compared to the MMST-based NRPMD method,[58] as shown in Fig. 4 (dashed lines).

Published under license by AIP Publishing

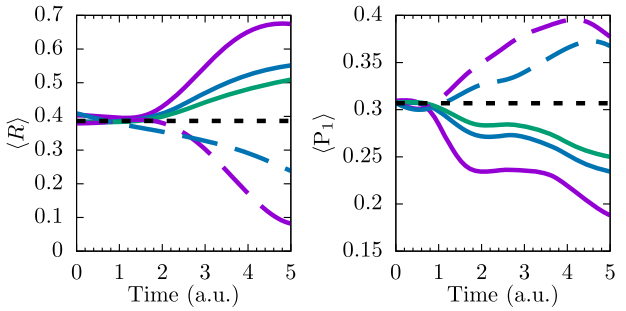

FIG. 7. Expectation values of the nuclear position operator (left panel) and the state 1 electronic population (right panel) for model IV (intermediate regime). The results are obtained from the SM-NRPMD method using $\{s \equiv Q, \bar{s} \equiv P\}$ (solid lines) and $\{s \equiv P, \bar{s} \equiv Q\}$ (dashed lines), with $N = 2$ (magenta lines), $N = 4$ (blue lines) and $N = 6$ (green lines) beads, respectively. The numerically exact results are shown in black dotted lines.

DATA AVAILABILITY

The data that support the findings of this study are available from the corresponding author upon reasonable request.

REFERENCES

[1] J. C. Tully, J. Chem. Phys. **137**, 22A301 (2012).
[2] J. C. Tully, J. Chem. Phys. **93**, 1061 (1990).
[3] J. E. Subotnik, A. Jain, B. Landry, A. Petit, W. Ouyang, and N. Bellonzi, Annu. Rev. Phys. Chem. **67**, 387 (2016).
[4] L. Wang, A. Akimov, and O. V. Prezhdo, J. Phys. Chem. Lett. **7**, 2100 (2016).
[5] R. Crespo-Otero and M. Barbatti, Chem. Rev. **118**, 7026 (2018).
[6] W. H. Miller, J. Phys. Chem. A **105**, 2942 (2001).
[7] W. H. Miller, J. Phys. Chem. A **113**, 1405 (2009).
[8] P. Huo and D. F. Coker, J. Chem. Phys. **135**, 201101 (2011).
[9] P. Huo and D. F. Coker, Mol. Phys. **110**, 1035 (2012).
[10] P. Huo, T. F. Miller, and D. F. Coker, J. Chem. Phys. **139**, 151103 (2013).
[11] M. K. Lee, P. Huo, and D. F. Coker, Annu. Rev. Phys. Chem. **67**, 639 (2016).
[12] H. Kim, A. Nassimi, and R. Kapral, J. Chem. Phys. **129**, 084102 (2008).
[13] A. Nassimi, S. Bonella, and R. Kapral, J. Chem. Phys. **133**, 134115 (2010).
[14] A. Kelly, R. van Zon, J. Schofield, and R. Kapral, J. Chem. Phys. **136**, 084101 (2012).
[15] C.-Y. Hsieh and R. Kapral, J. Chem. Phys. **138**, 134110 (2013).
[16] W. H. Miller and S. J. Cotton, Faraday Discuss. **195**, 9 (2016).
[17] S. J. Cotton and W. H. Miller, J. Chem. Phys. **150**, 104101 (2019).
[18] P. V. Parandekar and J. C. Tully, J. Chem. Theory Comput. **2**, 229 (2006).
[19] J. R. Schmidt, P. V. Parandekar, and J. C. Tully, J. Chem. Phys. **129**, 044104 (2008).
[20] S. Habershon and D. E. Manolopoulos, J. Chem. Phys. **131**, 244518 (2009).
[21] U. Müller and G. Stock, J. Chem. Phys. **111**, 77 (1999).
[22] B. J. Berne and D. Thirumalai, Annu. Rev. Phys. Chem. **37**, 401 (1986).
[23] D. M. Ceperley, Rev. Mod. Phys. **67**, 279 (1995).
[24] D. Chandler and P. G. Wolynes, J. Chem. Phys. **74**, 4078 (1981).
[25] S. Habershon, D. E. Manolopoulos, T. E. Markland, and T. F. Miller, Annu. Rev. Phys. Chem. **64**, 387 (2013).
[26] I. R. Craig and D. E. Manolopoulos, J. Chem. Phys. **121**, 3368 (2004).
[27] A. R. Menzeleev and T. F. Miller, J. Chem. Phys. **132**, 034106 (2010).
[28] A. R. Menzeleev, N. Ananth, and T. F. Miller, J. Chem. Phys. **135**, 074106 (2011).
[29] J. S. Kretchmer and T. F. Miller, J. Chem. Phys. **138**, 134109 (2013).
[30] J. S. Kretchmer and T. F. Miller, Inorg. Chem. **55**, 1022 (2016).
[31] R. L. Kenion and N. Ananth, Phys. Chem. Chem. Phys. **18**, 26117 (2016).
[32] N. Boekelheide, R. Salomón-Ferrer, and T. F. Miller, Proc. Natl. Acad. Sci. U. S. A. **108**, 16159 (2011).
[33] L. Wang, S. D. Fried, S. G. Boxer, and T. E. Markland, Proc. Natl. Acad. Sci. U. S. A. **111**, 18454 (2014).
[34] O. Marsalek and T. E. Markland, J. Phys. Chem. Lett. **8**, 1545 (2017).
[35] T. E. Markland and M. Ceriotti, Nat. Rev. Chem. **2**, 0109 (2018).
[36] J. O. Richardson and M. Thoss, J. Chem. Phys. **139**, 031102 (2013).
[37] J. O. Richardson, P. Meyer, M.-O. Pleinert, and M. Thoss, Chem. Phys. **482**, 124 (2017).
[38] S. N. Chowdhury and P. Huo, J. Chem. Phys. **150**, 244102 (2019).
[39] N. Ananth, J. Chem. Phys. **139**, 124102 (2013).
[40] S. Pierre, J. R. Duke, T. J. H. Hele, and N. Ananth, J. Chem. Phys. **147**, 234103 (2017).
[41] S. N. Chowdhury and P. Huo, J. Chem. Phys. **147**, 214109 (2017).
[42] H.-D. Meyer and W. H. Miller, J. Chem. Phys. **70**, 3214 (1979).
[43] G. Stock and M. Thoss, Phys. Rev. Lett. **78**, 578 (1997).
[44] M. Thoss and G. Stock, Phys. Rev. A **59**, 64 (1999).
[45] S. N. Chowdhury and P. Huo, J. Chem. Phys. **154**, 124124 (2021).
[46] N. Ananth and T. F. Miller, J. Chem. Phys. **133**, 234103 (2010).
[47] T. J. H. Hele and N. Ananth, Faraday Discuss. **195**, 269 (2016).
[48] J. R. Klauder, Phys. Rev. D **19**, 2349 (1979).
[49] H.-D. Meyer and W. H. Miller, J. Chem. Phys. **71**, 2156 (1979).
[50] A. Lucke, C. H. Mak, and J. T. Stockburger, J. Chem. Phys. **111**, 10843 (1999).
[51] A. Garg, E. Kochetov, K.-S. Park, and M. Stone, J. Math. Phys. **44**, 48 (2003).
[52] X. Song and T. van Voorhis, J. Chem. Phys. **124**, 134104 (2006).
[53] J. E. Runeson and J. O. Richardson, J. Chem. Phys. **151**, 044119 (2019).
[54] J. E. Runeson and J. O. Richardson, J. Chem. Phys. **152**, 084110 (2020).
[55] Quasi-distributions in quantum optics, in *A Group-Theoretical Approach to Quantum Optics*, edited by A. Klimov and S. Chumakov (John Wiley & Sons, 2009), Chap. 10, pp. 237–277.
[56] J. R. Mannouch and J. O. Richardson, J. Chem. Phys. **153**, 194109 (2020).
[57] J. R. Mannouch and J. O. Richardson, J. Chem. Phys. **153**, 194110 (2020).
[58] M. A. C. Saller, J. E. Runeson, and J. O. Richardson, "Path-integral approaches to non-adiabatic dynamics," in *Quantum Chemistry and Dynamics of Excited States* (John Wiley & Sons, 2020), Chap. 20, pp. 629–653.
[59] J. M. Radcliffe, J. Phys. A: Gen. Phys. **4**, 313 (1971).
[60] Y. Wu and J. E. Subotnik, Nat. Commun. **12**, 700 (2021).
[61] S. J. Cotton and W. H. Miller, J. Phys. Chem. A **119**, 12138 (2015).
[62] J. Liu, J. Chem. Phys. **145**, 204105 (2016).
[63] H. F. Trotter, Proc. Am. Math. Soc. **10**, 545 (1965).
[64] R. P. Feynman and A. R. Hibbs, *Quantum Mechanics and Path Integrals* (Dover Publications, Inc., 1965).
[65] C.-Y. Hsieh and R. Kapral, J. Chem. Phys. **137**, 22A507 (2012).
[66] M. H. Alexander, Chem. Phys. Lett. **347**, 436 (2001).
[67] J. R. Schmidt and J. C. Tully, J. Chem. Phys. **127**, 094103 (2007).
[68] T. J. H. Hele, "An electronically non-adiabatic generalization of ring polymer molecular dynamics," MChem thesis, Exeter College, University of Oxford, 2011.
[69] D. T. Colbert and W. H. Miller, J. Chem. Phys. **96**, 1982 (1992).
[70] T. J. H. Hele, M. J. Willatt, A. Muolo, and S. C. Althorpe, J. Chem. Phys. **142**, 134103 (2015).
[71] T. J. H. Hele, M. J. Willatt, A. Muolo, and S. C. Althorpe, J. Chem. Phys. **142**, 191101 (2015).
[72] X. He, Z. Gong, B. Wu, and J. Liu, J. Phys. Chem. Lett. **12**, 2496 (2021).
[73] S. J. Cotton and W. H. Miller, J. Chem. Phys. **150**, 194110 (2019).
[74] S. J. Cotton and W. H. Miller, J. Chem. Phys. **139**, 234112 (2013).
[75] M. S. Church, T. J. H. Hele, G. S. Ezra, and N. Ananth, J. Chem. Phys. **148**, 102326 (2018).

Published under license by AIP Publishing